Experimental and Computational Atomic Spectroscopy for Astrophysics

Oscillator strengths and lifetimes for Mg I, Si I, Si II, Sc I, and Sc II

Asli Pehlivan Rhodin

LUND
UNIVERSITY

Thesis for the degree of Doctor of Philosophy

Thesis advisors: Assoc. Prof. Henrik Hartman, Prof. Per Jönsson, Dr. Hampus Nilsson
Faculty opponent: Dr. Gillian Nave

To be presented, with the permission of the Faculty of Science of Lund University, for public criticism in the Lundmark lecture hall (Lundmarksalen) at the Department of Astronomy and Theoretical Physics on Thursday, 22nd of March 2018 at 09:00.

Organization
LUND UNIVERSITY
Department of Astronomy and Theoretical Physics
Box 43
SE-221 00 LUND
Sweden

Document name
DOCTORAL DISSERTATION

Date of issue
22 March 2018

Author(s)
Asli Pehlivan Rhodin

Sponsoring organization

Title and subtitle
Experimental and Computational Atomic Spectroscopy for Astrophysics
Oscillator strengths and lifetimes for Mg I, Si I, Si II, Sc I and Sc II

Abstract
Atomic data such as oscillator strengths and wavelengths are important for astrophysical applications as they have a crucial role in determining abundances of specific elements in a star, a galaxy, or any object emitting radiation in the space. Stars in the Galaxy mostly keep the composition of the interstellar gas from which they were formed, therefore studying stellar abundances helps us understand how the Milky Way was formed and how it evolved. However, atomic data of most chemical elements are incomplete and/or have low quality, particularly for the infrared wavelength region and for the highly excited levels.
This PhD project focuses on completing missing atomic data for the infrared region in addition to the optical and UV regions, and improving the existing data. In order to achieve this, I have performed both laboratory measurements and large scale atomic structure calculations.
Experimental oscillator strengths have been derived by combining measured branching fractions with radiative lifetimes. A hollow cathode discharge lamp has been used as a light source to produce free atoms in a plasma and a Fourier transform spectrometer has recorded the intensity-calibrated high-resolution spectra. In addition, atomic structure calculations have been performed using the multiconfiguration Hartree-Fock programmes ATSP2K and GRASP2K to determine oscillator strengths and lifetimes. Combining the experimental work with the computational approach allows determining a large set of accurate and validated atomic data.
In this thesis, an evaluated set of atomic data for Mg I, Si I, Si II, Sc I, and Sc II has been provided for astrophysical applications. The experimental oscillator strengths in the infrared region have been measured for the first time. The uncertainties in the experimental oscillator strengths are as low as 5% for strong transitions. The theoretical oscillator strengths are validated with the experimental values and with internal investigations of the length and velocity forms. The small uncertainties in the values allow accurate astrophysical abundance determinations within the 0.1dex uncertainty.

Key words
atomic data, methods: laboratory: atomic – techniques: spectroscopic, methods: numerical

Classification system and/or index terms (if any)

Supplementary bibliographical information

Language
English

ISSN and key title

ISBN
978-91-7753-533-1 (print)
978-91-7753-534-8 (pdf)

Recipient´s notes

Number of pages
139

Price

Security classification

Experimental and Computational Atomic Spectroscopy for Astrophysics

Oscillator strengths and lifetimes for Mg I, Si I, Si II, Sc I, and Sc II

Asli Pehlivan Rhodin

LUND
UNIVERSITY

Faculty Opponent

Dr. Gillian Nave
National Institute of Standards and Technology, NIST
Gaithersburg, USA

Evaluation Committee

Prof. Anja C. Andersen
Niels Bohr Institute
University of Copenhagen

Prof. Matthew Stanley Johnson
Department of Chemistry
University of Copenhagen

Assoc. Prof. Rolf Jonas Persson
Department of Teacher Education
Norwegian University of Science and Technology

Front cover: A spectrum of magnesium recorded with the high-resolution Fourier transform spectrometer (FTS), Bruker IFS 125 HR, in the Edlén Laboratory, at Lund Observatory.
Back cover: An image of "Pillars of Creation", the Eagle Nebula, image credits: NASA, ESA and the Hubble Heritage Team (STScI/AURA).

Faculty of Science, Department of Astronomy and Theoretical Physics
ISBN: 978-91-7753-533-1 (print)
ISBN: 978-91-7753-534-8 (pdf)

Printed in Sweden by Media-Tryck, Lund University, Lund 2018

MALMÖ
UNIVERSITY

Department of Materials Science and Applied Mathematics
Faculty of Technology and Society, Malmö University
SE 20506 Malmö
http://www.mau.se

To my husband, Annem, Babam ve Can'a

Contents

List of publications

This thesis is based on the following publications:

I **Laboratory oscillator strengths of Sc I in the near-infrared region for astrophysical applications**

A. Pehlivan, H. Nilsson, H. Hartman (2015)
Astronomy & Astrophysics, vol. 582, A98 (8 p.)

II **Experimental and theoretical oscillator strengths of Mg I for accurate abundance analysis**

A. Pehlivan Rhodin, H. Hartman, H. Nilsson, P. Jönsson (2017)
Astronomy & Astrophysics, vol. 598, A102 (12 p.)

III **Lifetime measurements and oscillator strengths in singly ionized scandium and the solar abundance of scandium**

A. Pehlivan Rhodin, M.T. Belmonte, L. Engström, H. Lundberg, H. Nilsson, H. Hartman, J.C. Pickering, C. Clear, P. Quinet, V. Fivet, P. Palmeri (2017)
Monthly Notices of the Royal Astronomical Society, vol. 472, 3337 (17 p.)

IV **Accurate and experimentally validated transition data for Si I and Si II**

A. Pehlivan Rhodin, H. Hartman, H. Nilsson, P. Jönsson (2018)
In manuscript

Publications not included in this thesis:

I **Abundances of disk and bulge giants from high-resolution optical spectra. I. O, Mg, Ca, and Ti in the solar neighborhood and Kepler field samples**

H. Jönsson, N. Ryde, T. Nordlander, **A. Pehlivan Rhodin**, H. Hartman, P. Jönsson, K. Eriksson (2017)
Astronomy & Astrophysics, vol. 598, A100 (11 p.)

Popular summary

Just after the Big Bang, there were only three elements; hydrogen, helium, and a small amount of lithium. The first generation stars were born in a cloud of these elements. When these stars died, they exploded as supernovae and ejected heavier elements into the interstellar medium. The next generation stars were formed from this enriched medium, and therefore they had more metals. Consecutive cycles of birth and death of stars enrich the universe with more metals. Stars with low mass, such as our Sun, produce several light elements during nuclear burning phases and a range of neutron-capture elements due to slow neutron-capture reactions in their interiors. These elements are enriched into the stellar atmospheres when they are dredged-up to the surfaces during the asymptotic giant branch (AGB) phase, before becoming planetary nebulae. During the planetary nebula phase, their outer layers are ejected by the stellar winds and the remaining core is called a white dwarf. Massive stars can produce elements up to iron during their lifetimes and heavier elements are formed while they explode as supernovae at the end of their lives.

Most of the information we have about stars, is hidden in their light. Astronomers analyse the light from stars to understand which atoms and molecules are present in stars and the abundance of these species. As stars in the Galaxy mostly keep the composition of the interstellar medium in which they were born, these analyses help us to construct the evolution history of our Galaxy. To analyse the light, atomic data such as wavelengths and oscillator strengths of transitions are fundamental. However, atomic data of some elements are incomplete and/or have low quality, in particular in the infrared region. This, in turn, makes it difficult to study the galactic evolution with infrared spectra. My work has been aimed at providing the missing atomic data and improving the existing data, primarily focusing on the oscillator strengths.

To accomplish this, I have performed experimental work and atomic structure calculations. Experimental measurements have been conducted in the Edlén laboratory at the Astronomy building in Lund, at the High Power Laser Facility at the Physics Department in Lund, and in the Blackett laboratory at Imperial College in London using a high-resolution Fourier transform spectrometer, a hollow cathode discharge lamp, and lasers. In the laboratory a plasma of the element that is of interest can be created. By studying the light from this plasma, one can derive atomic parameters, such as oscillator strengths, which are related to the strengths of spectral lines, or radiative lifetimes, which are lifetimes of atomic levels before they decay to lower levels. In cases where different wavelength regions are not accessible simultaneously with the experimental setup, calculations complement missing atomic parameters regardless of the wavelength region. Calculations in this thesis have been performed using large scale atomic structure computer packages, ATSP2K or GRASP2K, to compute the atomic parameters of interest.

An extensive set of accurate atomic data for a large wavelength region is obtained by performing both experiments and calculations. The experimental results, which have small uncertainties, agree well with the previous measurements in the optical region and/or with the calculations of the current work. In addition, theoretical calculations complement the experimental values for the unobserved and uncertain transitions. The provided wavelengths help obtaining the elemental composition, and oscillator strengths and transition rates can be used to determine the elemental abundances in stars, nebulae, or even planetary atmospheres.

Populärvetenskaplig sammanfattning

Precis efter Big Bang fanns endast tre grundämnen: väte, helium och en liten mängd litium. De första stjärnorna föddes i gasmoln som innehöll dessa ämnen. När den första generationen stjärnor i slutet av sina liv exploderade som supernovor spreds de tyngre grundämnena som tillverkats ut i det interstellära mediet. Nästa generations stjärnor bildades från detta berikade medium, och innehöll därför fler metaller. Fortsatta cykler av födsel och död av stjärnor berikar universum med högre ymnighet av metallerna. I stjärnor med liten massa, som vår sol, bildas flera lättare ämnen i stjärncentrum, medan neutroninfångningsämnen på grund av långsamma neutroninfångningsreaktioner bildas i stjärnornas inre. Dessa ämnen berikar stjärnatmosfären när de förflyttas upp till ytan under den så kallade AGB-fasen, innan stjärnan blir en planetarisk nebulosa. Under denna fas skickas stjärnans yttre lager ut av stjärnvindarna och resterande kärna kallas en vit dvärg. Stjärnor med stor massa kan producera ämnen upp till järn under sina livstider och tyngre ämnen bildas medan de exploderar som supernovor i slutet av sina liv.

Majoriteten av informationen vi har om stjärnor är dold i deras ljus. Astronomer analyserar ljuset från stjärnor för att förstå vilka atomer och molekyler som finns och i vilka ymnigheter de finns i stjärnorna. Eftersom stjärnor i vår galax oftast avspeglar det interstellära medium där de föddes kan analysen av stjärnornas ljus fungera som ett verktyg för att konstruera den evolutionära historien för Vintergatan. För att analysera ljuset är atomära data såsom våglängder och oscillatorstyrkor för övergångar grundläggande. För vissa element är emellertid dessa data ofullständiga eller av låg kvalitet, särskilt i det infraröda området. Detta gör det i sin tur svårt att studera den galaktiska utvecklingen med hjälp av infraröda spektra. Mitt arbete har varit inriktat på bestämma saknad atomdata och förbättra befintliga data, med fokus på oscillatorstyrkor.

Teknikerna har varit både experimentella och beräkningsbaserade. Experimentella mätningar har utförts vid Edlén-laboratoriet vid den astronomiska institutionen, Lund High Power Laser Facility vid Fysikinstiutionen vid Lunds universitet samt Blackett Laboratory vid Imperial College i London. Vi har använt högupplösande Fourier-transformationsspektrometrar med en hålkatodurladdningsljuskälla samt pulsade lasrar för att mäta livstider. I laboratoriet har vi skapat plasmor med de grundämnen som vi vill studera. Genom att studera ljuset från dessa plasmor har de atomära parametrar, såsom oscillatorstyrkor som relaterar till linjernas inre styrka, och livstider som relaterar till populationen hos atomära tillstånd innan de faller ner till lägre nivåer, bestämts. I de fall där övergångar faller i våglängdsområden som inte experimentinställningen är känslig för eller för tillstånd som inte populeras, har vi använt beräkningar för att komplettera saknade atomparametrar. Genom att utföra storskaliga atomstrukturberäkningar med hjälp av programpaketen ATSP2K och GRASP2K kan vi bestämma atomparametrar noggrant.

En omfattande uppsättning noggranna atomdata för ett stort våglängdsintervall har uppnåtts genom att kombinera experiment och beräkningar. De experimentella resultaten, vilka har små osäkerheter, överensstämmer väl med de tidigare mätningarna i det synliga området och med beräkningar i det aktuella arbetet. Dessutom kompletterar teoretiska beräkningar experimentella värden för ej observerade eller osäkra övergångar. De rapporterade våglängderna hjälper till att erhålla den kemiska sammansättningen, medan oscillatorstyrkor och övergångsstyrkor kan användas för att bestämma ymnigheterna i stjärnor, nebulosor eller till och med planetatmosfärer.

Acknowledgements

These last four years, I have had an amazing journey. Along this journey, I have met many wonderful people who directly or indirectly expanded my horizon both professionally and socially. First of all, I would like to thank all of my three supervisors for their guidance, patience, ethical insight, support, and enthusiasm about science. Thank you Henrik Hartman for supporting me, sharing your knowledge, respecting my ideas, listening to me about both work-related and unrelated issues, and training me to become a great scientist like yourself. Per Jönsson, with your passion for science, you made computational atomic physics such an interesting subject, thank you for the time and effort you spent on my education and for patiently answering all of my questions. Hampus Nilsson, thank you for preparing me for the laboratory, making atomic spectroscopy an exciting topic and your advices through out the years. I am very lucky to have met you all and to have had you as my supervisors. I have learned how to be a scientist from the best.

I would like to thank all the staff, PhD and masters students, and people who have passed through the Astronomy Department in the last years, you have all contributed to make this journey a memorable one. Special thanks goes to Nils Ryde, Henrik Jönsson and Brian Thorsbro for their interest in atomic data and many scientific discussions we have had. During these four years, I have shared my office with different people. A big applause to my office mates with whom I not only have shared the same office, but also have had so much fun! The office B237D has been honoured by Henrik J., Simona, Katrin and its new member, Madeleine. Thank you for these fantastic years. In addition, I wish to acknowledge all the Malmö University co-workers and especially Mats Persson for the help provided regarding my employment at MAU.

I am delighted that I had the chance to visit the Imperial College spectroscopy group: Juliet Pickering, Teruca Belmonte, and Christian Clear. Thank you for taking care of me when I visited the Blackett laboratory in London and for the successful collaboration. I have had a fantastic time collaborating with you. Moreover, I would like to express my gratitude to all co-authors in my four research papers and to acknowledge the grant from the Swedish Research Council (VR) that financed my employment and the travel grant from the Royal Physiographic Society of Lund.

Many thanks to the Lund-Malmö Centre for Atomic Systems (LUMCAS) group: Lars, Hans, Jörgen, Tomas, Sven, Stefan, Rickard, Asimina, Jon, Betül, and Lennart for providing a very professional and at the same time very friendly atmosphere with fruitful discussions.

Many hugs to my sister from another mister, Johanna P., for always being there for me, either to celebrate or to forget. And last but not least, my sincere gratitude to my mom, dad, brother, and my family in Sweden, Åsa, Bengt, Gunnel, Johanna, and Christian for their endless support and love. Without my dearest husband, Henrik, I would not have completed this journey. Thank you for EVERYTHING from being so patient to your encouragement at every moment, and thank you for loving me and believing in me. Blue whales cannot describe enough how grateful I am to have you on my side.

Part I

Research context

Chapter 1

Introduction

1.1 Connection between astrophysics and atomic physics

Essentially all information about astrophysical objects, in our Galaxy and beyond, is derived from the radiated light from these objects. The light from stars approximately follows a blackbody radiation distribution for which the peak wavelength depends on the temperature of the stellar atmosphere. Imprinted on this emitted radiation is absorption features from atoms and molecules in the stellar atmosphere. Absorption features in a blackbody spectrum tell us which atoms are present and the amount of them in the star. This light, however, cannot be fully interpreted, if the properties of atoms (and sometimes molecules) are not well known.

The absorption features were first discovered by Joseph von Fraunhofer in 1814 as dark lines in the solar spectrum, see Figure 1.1 for an example of such absorption features. He was not able to explain the origin of these lines, but labeled them with the letters in the alphabet (von Fraunhofer 1817). For instance, the sodium D lines, and the calcium H and K lines, are still used with the same labels by astronomers. In the 1850s Kirchhoff & Bunsen showed that these dark lines, which had emission counterparts in laboratory flames, arose from different chemical elements. In other words, each element had unique spectral lines, like "fingerprints". Kirchhoff & Bunsen were able to identify some of the Fraunhofer lines in the solar spectra from their laboratory experiments. In 1888, J. Rydberg developed a formula that predicted the wavelength of spectral lines. This formula was based on fitting a general function that generated all wavelengths of hydrogen-like ele-

ments. However, it had no physical explanation. The relation between atoms and spectral lines could not be explained completely until the introduction of quantum mechanics in the beginning of the 20th century.

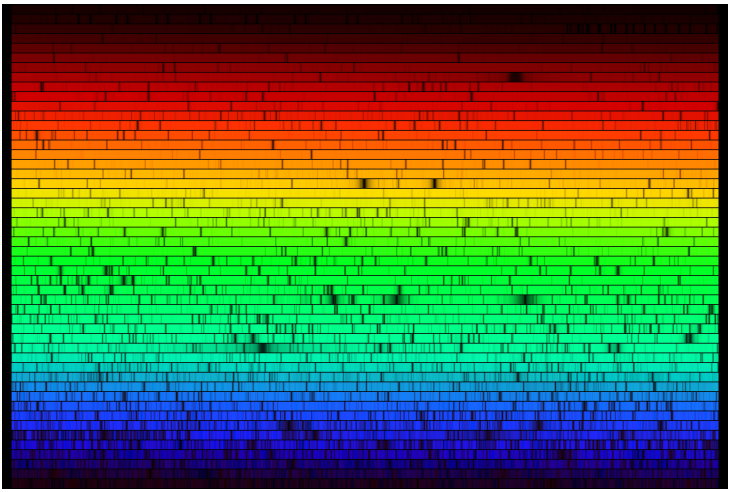

Figure 1.1: High resolution solar spectrum in the optical wavelength region that was observed with the Fourier Transform Spectrometer at the McMath-Pierce Solar Facility at the National Solar Observatory on Kitt Peak. Dark lines are the absorption features from various elements present in the solar atmosphere. In the courtesy of N.A.Sharp, NOAO/NSO/Kitt Peak FTS/AURA/NSF.

The evolution of the atomic theory, as outlined in Hartree (1957), started with the discovery of the electron by Thomson (1897). Following that, Rutherford (1911) discovered the atomic nucleus, surrounded with electrons, by showing that most of the mass and the positive charge were accumulated in a region very small relative to the size of the entire atom. With the classical mechanical approach, the electrons would radiate energy and collapse into the nucleus in a very short time scale. Bohr (1913) improved Rutherford's theory by introducing Planck's theory of "the elementary quantum of action". In his model, electrons were in stable orbits around the nucleus (or stable energy states), and only emitted or absorbed light when they moved between discrete energy states. Moreover, he assumed that electrons were in these stationary states in the field of the nucleus and other electrons. Other improvements were the electron spin concept formulated by Uhlenbeck & Goudsmit (1925) and Pauli's exclusion principle, which stated that two electrons could not

have the same quantum numbers n, l, m_l, m_s. Finally, Schrödinger (1926) developed wave mechanics following the idea of de Broglie (1925)'s concept of wave systems, which resulted in formulation of the Schrödinger's equation. The solutions to the Schrödinger's equation are the wavefunctions. They describe atomic states and can be determined using appropriate approximations as discussed in the further chapters.

With the help of quantum (wave) mechanics, astrophysical spectral lines can be

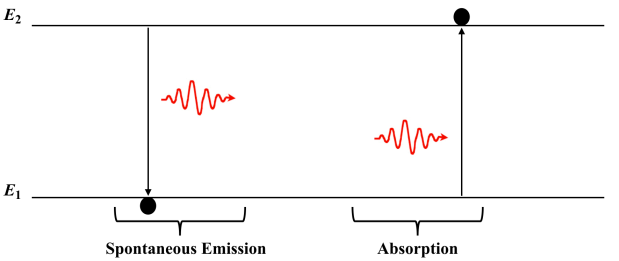

Figure 1.2: Schematic figure of two types of radiative transitions.

explained. Observed astrophysical spectral lines result from the transitions between energy levels of an atomic system. These transitions occur by absorbing or emitting photons. There are two types of transitions important for astrophysical analyses as shown in Figure 1.2. The first one is called the spontaneous emission, which happens when an atom in the excited level, E_2, decays to the lower level, E_1, by emitting a photon that has the same energy as the difference between the upper and lower levels, $E_2 - E_1$. The other one is called absorption, which takes place when an atom moves to the upper level, E_2, from the lower level, E_1, by taking the energy of a photon that is exactly equal to the energy difference between the upper and lower levels. Observationally these transitions correspond to two different cases:

- If one examines the light from a hot thin gas cloud, only the emitted wavelengths from that source will be visible, hence an emission spectrum, as in nebulae spectra.
- If one gathers the light from a hot opaque object blocked by a thin cooler gas cloud, a continuous spectrum with absorption lines is observed, as in most of the stellar spectra.

Additionally, if one observes a hot opaque source, for example a star with no atmosphere, the collected light from this source will give a continuous spectrum, in other words, one can see light in all wavelengths as in a blackbody spectrum. In either type of spectra, the presence of spectral lines, the fingerprints of an atom, tells us about the composition of an object. On the other hand, the amount of the emitted light, or the amount of the absorbed light, tells us about the quantity of atoms in an object. To convert the observed absorption to an abundance, one needs to know the atomic oscillator strength and create a model of the stellar atmosphere. Figure 1.3 shows an example of an absorption spectrum. In this figure, the position of an absorption line answers the question of which element gives rise to this line, and the depth, or equivalent width, of the line gives information about the amount of this element in the source.

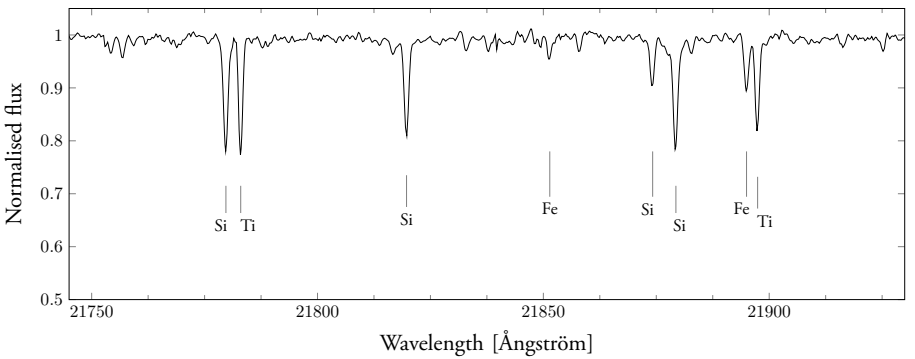

Figure 1.3: Example of an absorption spectrum. The position/wavelength of the lines is related to a specific element whereas the depth of the lines tells about the amount of that element. Figure from Thorsbro (2016).

The connection between the stellar element abundance and the oscillator strength, for a weak line is given by the equation below (Gray 2005),

$$\log\left(\frac{EW}{\lambda}\right) = \log(Abundance) + \log(\lambda g f) + C + \text{other parameters} \quad (1.1)$$

where EW is the equivalent width of the spectral line, which is directly determined from an observed spectrum and is the width of a rectangle that has the same area as the area between the spectral line and the continuum level, λ is the wavelength of the spectral line, g is the statistical weight of the lower level (atomic parameter), f is the oscillator strength, known as the f-value, and the constant

C and other parameters are not important at this point. The projects in this thesis are focused on determining the f-value and this value is an atomic parameter related to the intrinsic strength of a transition. As seen from Eq. 1.1, the derived abundance depends on an accurate measurement of the equivalent width and on the use of high-quality atomic data. If the $\log(gf)$ value is incorrect by 0.5 dex (decimal exponent, notation for $10^{0.5}$), approximately by a factor of three, and other parameters are fixed, this will cause an overestimate/underestimate of the true abundance by 0.5 dex. Therefore, it is important to have correct and accurate $\log(gf)$ values. Stellar spectroscopists aim at abundance analyses with uncertainties smaller than 0.1 dex. This, in turn, motivates us to provide $\log(gf)$ values with small uncertainties, roughly a maximum of 0.1 dex. This uncertainty in $\log(gf)$ values corresponds to a 25% relative uncertainty in f-values. In the present thesis, this goal is achieved with uncertainties as low as 5%, corresponding to 0.02 dex in $\log(gf)$ values.

1.2 Astrophysics and the need for accurate and complete atomic data

Analysing stellar spectra helps us to understand in what environments stars are born. This, in turn, helps us to find out the formation and evolution of our own Galaxy. As discussed in the previous section, the interpretation of stellar spectra relies on high-quality atomic data. For this purpose, there are several groups making line lists with the best available atomic data (Piskunov et al. 1995; Heiter et al. 2015; Shetrone et al. 2015; Thorsbro 2016; Ryde et al. 2016). Yet, there is still a need of additional and more accurate atomic data. The new generation advanced astrophysical instruments have improved the quality of the observed astrophysical spectra and opened up new wavelength regions, which, in turn, requires ever increasing accuracy on the atomic parameters and the stellar models .

The CRIRES+ at VLT will operate (2018) in the infrared region with a resolving power of $50\,000 - 100\,000$ (Dorn et al. 2014). The APOGEE-2 survey (Zasowski et al. 2017) observes in the infrared region with two different telescopes: the Sloan Foundation Telescope at Apache Point Observatory and the Irénée du Pont Telescope at Las Campanas Observatory in Chile (in the southern hemisphere and in the northern hemisphere, respectively) aiming at an elemental abundance precision of 0.1 dex. The Gaia-ESO (Gilmore et al. 2012) survey observes in the optical region with FLAMES at VLT, which has two different spectrographs: GIRAFFE

with intermediate or high resolution and UVES with high resolution (Pasquini et al. 2002). The 4MOST survey will start operating in 2021 and plan to observe 25 million stars in a five year period in the optical region (de Jong et al. 2016; Feltzing et al. 2017), and not to mention the HST's STIS (Riley 2017) that has been operating since 1997 (with a break between 2004-2009) with a high spatial resolution echelle spectroscopy in the UV region.

The common request of these instruments is the improved atomic data for the analyses of astrophysical spectra from the infrared region to the UV region. In particular in the infrared region, there are many observed lines, but the atomic data needed to identify and to analyse many of these lines are missing. Improved atomic data in this region is one of the achievements that has been accomplished with the research presented in this thesis. For example, there were no experimental Sc I oscillator strengths in the infrared region before Paper I and only three laboratory oscillator strengths of Mg I were known before Paper II. In addition, the lifetimes of the highly excited levels of Sc II have been measured for the first time in Paper III. An extensive set of high-quality oscillator strengths of the Si I and Si II lines has been lacking until Paper IV. Furthermore, a gravitational-wave and an associated γ-ray burst were detected simultaneously in August 2017, which boosted interest is the neutron star mergers. These events are thought to be the production site of many of the heavy elements, and the analysis of the ejecta can put light on the chemical yield from these events. A recent study of a kilonova spectrum, associated with a gravitational-wave source and γ-ray burst, found signatures of r-process elements (heavy elements that only form with rapid neutron capture) production. However, there is a lack of atomic data preventing these elements from being identified in the ejecta (Pian et al. 2017). Common for all of the above is that with the development of new instruments and state-of-the-art science exploring new territories, there is a great demand for high-quality atomic data. The urgent need of atomic data has been pointed out in a Nature (2013) editorial as one of the low-cost but high priorities for new observations.

1.3 Determination of atomic data

Atomic data needed for astrophysical spectral analyses, specifically wavelengths and oscillator strengths, can be derived from high-resolution experiments or can be calculated with atomic structure state-of-the-art codes, such as ATSP2K (Froese Fischer et al. 2007) and GRASP2K (Jönsson et al. 2017). The strength of this the-

sis is to use and combine both methods, and thereby provide the combination of experimental and calculated atomic data.

Both methods have their own strengths and limitations for the atoms and ions we study in the thesis, i.e. the neutral and singly ionised ions. It is more accurate to determine wavelengths and energy levels from experiments. However, the number of lines accessible is limited by the difficulties to populate highly excited levels and to detect lines appearing in different wavelength regions simultaneously. The importance of the latter is due to the fact that all the lines from the same upper energy level should be observed in order to derive the oscillator strengths, as explained in Chapter 2. On the other hand, if the lines from the same upper level are close in wavelength, the branching fractions can be determined with very small uncertainties since the uncertainty from the calibration basically disappears, and the main limitation is the lifetime uncertainties.

Calculations are able to provide values for lines that are not easily accessed in experiments. They have no limitations on the wavelength range, and the oscillator strengths can often be determined accurately for atomic systems that are not too complicated. The challenge for the calculations is to find accurate representations of the wavefunctions of the targeted states. The concern is the computational limitations. For example, large computational power is needed for calculations including highly excited atomic states or heavy atoms with low ionisation stages. The comparisons of calculated values with experimental values give an indication of the accuracy of the combined atomic data set. In addition, internal consistency of the calculations helps estimating uncertainties of the computed values, as discussed in Section 3.8.

Chapter 2

Measurements of atomic parameters

Atomic parameters, which are important for astrophysical applications are *energy levels*, *wavelengths*, *radiative lifetimes*, *transition probabilities*, and *oscillator strengths*. Energy levels cannot be observed directly but, the difference between two energy levels can be measured and is given by, $\Delta E = hc/\lambda$, where h is Planck's constant, c is the velocity of light and λ is the wavelength of the corresponding photon. In spectroscopy, wavenumbers are commonly used and related to wavelengths by $\sigma = 1/\lambda$ with a unit of cm^{-1}. Since only energy level differences are measurable, knowing the energy level structure of an atom is crucial to predict the wavelengths of transitions. The energy level structure is constructed relative to the ground level (the lowest possible level). For this reason, the ground level is set to zero energy to make all excited levels have positive energy values (Thorne et al. 1999). Figure 2.1 shows an example of a partial energy level diagram presenting the levels with $3snl$ configurations of neutral magnesium up to $n = 7$. The energy values are from the references in Martin & Zalubas (1980). The horizontal dashed line shows the ionisation limit for neutral magnesium, Mg I, which is at the same time the ground level of singly ionised magnesium, Mg II. The x-axis displays the terms with their corresponding levels in the same column and these labels are based on the quantum numbers: the total orbital momentum and the total spin momentum quantum numbers, L and S, respectively. The y-axis is energy values in cm^{-1}. The ground level of Mg I is 3s^2 ^{1}S$_0$ and energy needed to move an electron from the ground level to an excited level, such as 3s3p ^{1}P$_1$, is called the excitation energy. From energy levels in a diagram, possible transitions are predicted. The

transitions from excited levels in Mg I, reported in Paper II, are marked with the dashed lines in the figure. The unobserved lines either have very low transition probabilities or the upper level they radiate from is not populated enough or are out of the instruments wavelength range, to be described later.

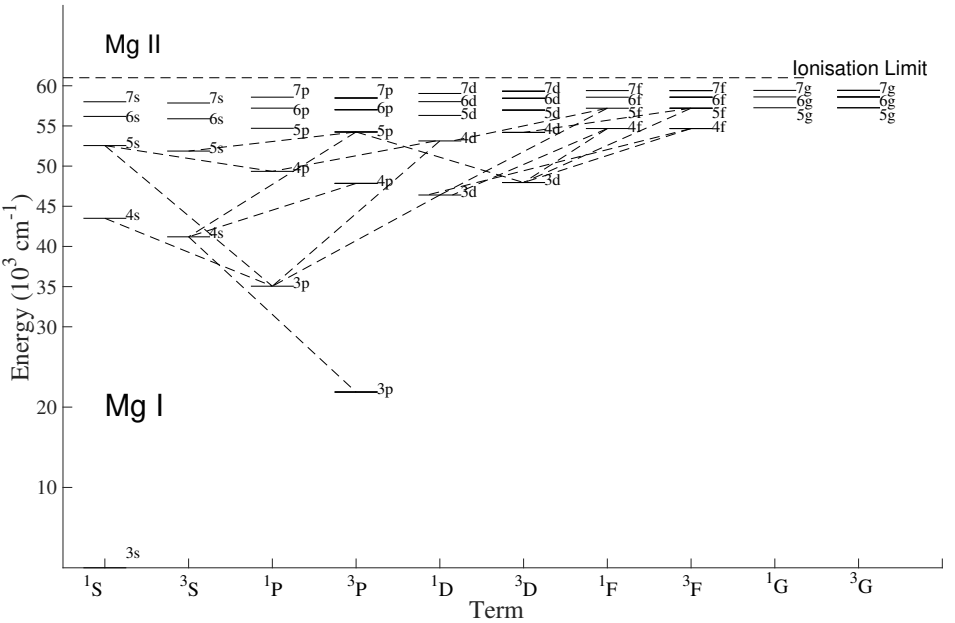

Figure 2.1: Partial energy level diagram of Mg I. On the x-axis, configurations with the same term grouped together and y-axis shows the corresponding energy values. Transitions from all the levels shown in this diagram have been calculated in Paper II. In addition, dashed lines show the transitions that have been measured in Paper II.

There are three types of bound-bound radiative transitions: absorption, spontaneous emission, and stimulated emission. In the experimental part of the projects in this thesis, only spontaneous emission is considered. However, one should keep in mind that the absorption is observed in most of the stellar spectra, whereas nebular spectra show emission features, as explained in Section 1.1.

Oscillator strengths have an important role in the determination of elemental abundances in stars and they are used in absorption line analyses. The goal of the projects in this thesis has been to determine this parameter for a large number of transitions for various atoms. The f-value is a measure of the intrinsic strength of a transition and is related to the transition probability, $A_{\rm ul}$, by,

$$f = \frac{g_{\rm u}}{g_{\rm l}} \frac{\varepsilon_0 m c^3}{2\pi e^2 \nu^2} A_{\rm ul}, \tag{2.1}$$

where $g_{\rm u}$ and $g_{\rm l}$ are the statistical weights of the upper, (u), and lower levels (l), respectively, ε_o is the permittivity of vacuum, m is the electron mass, e is the elementary charge and ν is the frequency of the transition (Thorne et al. 1999). In order to determine the f-value, one should know the transition probability, $A_{\rm ul}$ value, of the transition which is a measure of strength of emission lines.

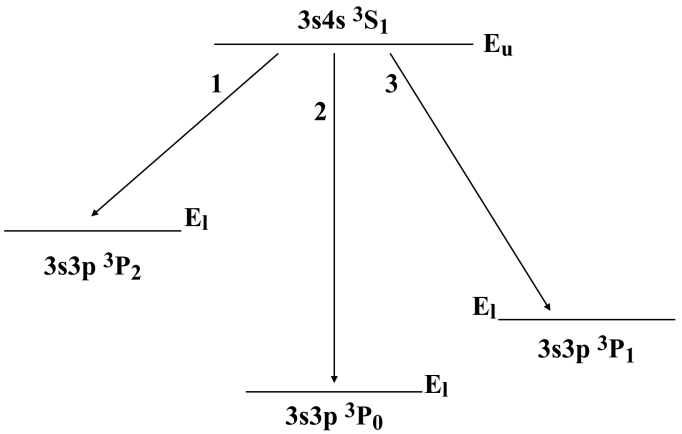

Figure 2.2: Example of possible decay channels from the upper level, 3s4s ^{3}S$_1$, of Mg I.

The branching fraction of a line is defined as the transition probability of the emission line divided by the sum of transition probabilities of all emission lines from the same upper level (Huber & Sandeman 1986),

$$BF_{\rm ul} = \frac{A_{\rm ul}}{\sum_i A_{{\rm u}i}}. \tag{2.2}$$

For example, the branching fraction of the "transition 1", 3s3p ^{3}P$_2$ - 3s4s ^{3}S$_1$, in Figure 2.2 is $BF_1 = \frac{A_1}{A_1+A_2+A_3}$. For an optically thin plasma, the intensity of an emission line is proportional to the population of the upper level, N_u, the statistical weight of the upper level, and the transition probability of the transition, $I_\mathrm{ul} \propto N_\mathrm{u} g_\mathrm{u} A_\mathrm{ul}$. As all the lines decay from the same upper level, N_u and g_u are the same for all lines and the BF simply becomes the relative intensity ratio, $BF_\mathrm{ul} = I_\mathrm{ul} / \sum_i I_{\mathrm{u}i}$. Thus, it is possible to derive BFs by measurements of relative intensities of all transitions from the same upper level. The integrated intensities of the observed lines have been determined by the FTS analysis software `GFit` (Engström 1998, 2014). However, observation of all lines from the same upper level can be problematic if the lines decay in different wavelength regions, such as infrared and UV, or if some of the lines are too weak to be detectable. These issues can be resolved with the help of theoretical calculations which make it possible to predict contributions from missing lines to the sum of transition probabilities.

The A_ul value can be derived from the experimentally determined BF and the lifetime of the upper level, τ_u,

$$A_\mathrm{ul} = \frac{BF_\mathrm{ul}}{\tau_\mathrm{u}}. \tag{2.3}$$

Since a BF is a relative intensity ratio, it has no units and a lifetime has a unit of s. As a result, the unit of A_ul is s^{-1}.

The radiative lifetime of a level is the expected time that an atom spends in an excited level before it decays to a lower level via spontaneous emission. It is related to the sum of transition probabilities from the same upper level by,

$$\tau_\mathrm{u} = \frac{1}{\sum_i A_{ui}}, \tag{2.4}$$

which means that the transition probabilities of all possible decays from the same upper level contribute to the lifetime of that level. For example, the lifetime of the Mg I level 3s4s ^{3}S$_1$ in Figure 2.2 can be computed from $\tau = \frac{1}{A_1+A_2+A_3}$. This parameter can be measured using different techniques such as the time resolved laser induced fluorescence or beam foil. In Paper III, the two-step time resolved laser induced fluorescence (TR-LIF) method has been used as described in Section 2.2.

Table 2.1: Selection rules for E1, M1, and E2 transitions.

E1	M1	E2
General rules independent from the labelling scheme		
Parity change	No parity change	No parity change
$\Delta J = 0, \pm 1$	$\Delta J = 0, \pm 1$	$\Delta J = 0, \pm 1, \pm 2$
$(J = 0 \nrightarrow 0)$	$(J = 0 \nrightarrow 0)$	$(J = 0 \nrightarrow 0, 1; 1/2 \nrightarrow 1/2)$
LS coupling rules		
$\Delta S = 0$	$\Delta S = 0$	$\Delta S = 0$
$\Delta L = 0, \pm 1$	$\Delta L = 0$	$\Delta L = 0, \pm 1, \pm 2$
$(L = 0 \nrightarrow 0)$		$(L = 0 \nrightarrow 0, 1)$

The dominant type of radiation is the electric dipole radiation (E1). In an E1 transition, an odd parity level can decay only to an even parity level, and vice verse. The parity of an atomic state can be derived by, $P = (-1)^{\sum_i l_i}$, where l is the orbital momentum quantum number for each electron in an N-electron system, and $P = 1$ or -1 means even or odd parity, respectively. The strongest E1 transitions connecting the ground level to the opposite parity low excitation levels are called the resonance lines. Following the E1 transitions, the magnetic dipole (M1) transitions and the electric quadruple (E2) transitions are important. They are the transitions which connect levels with the same parity. These transitions are not allowed by E1 transitions, and thus the corresponding lines are called forbidden. Forbidden lines are much weaker than the lines from E1 transitions, and thus the upper levels have several orders of magnitude longer lifetimes in neutral and near-neutral atoms. For example, the M1 transition $2s^2 2p^2\ ^3P_1 - 2s^2 2p^2\ ^3P_2$ in [OIII] has a transition probability of 9.7×10^{-5} s^{-1} (Galavis et al. 1997) and the E2 transition $2s^2 2p^2\ ^3P_0 - 2s^2 2p^2\ ^1D_2$ in [OIII] has a transition probability of 1.7×10^{-6} s^{-1} (Galavis et al. 1997) (note that this transition does not follow a pure LS coupling, therefore the spin change rule is relaxed), whereas the E1 transition probability of the $2s^2 2p^2\ ^3P_2 - 2s2p^3\ ^3P_2^o$ transition is 1.4×10^9 s^{-1} (Nussbaumer & Storey 1981). In addition to the parity rule, there are other constrains including the total angular momentum change and the LS coupling rules, e.g. E2 transitions can occur between states with larger difference in J, compared to M1 transitions. These rules are given in Table 2.1 (Cowan 1981).

2.1 Experimental setup for BF measurements

Transition probabilities and f-values can be measured with different methods. In the projects of this thesis, I have combined radiative lifetimes with BFs to determine f-values. For some projects available experimental lifetimes from the literature and for others the calculated lifetimes have been combined with the experimental BFs. The BF measurements have been performed using a hollow cathode discharge lamp as a light source and a Fourier transform spectrometer to record the spectra. Equipments that have been used during the measurements and the experimental set-up are described briefly below.

2.1.1 Hollow cathode discharge lamp

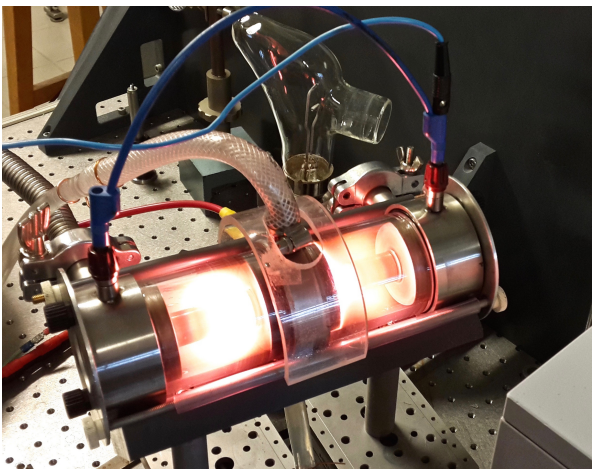

Figure 2.3: Picture of the hollow cathode lamp built in Lund.

A hollow cathode discharge lamp (HCL) has been used to produce plasma of different atoms and ions. The HCL in the present project is a custom-made glass tube with anodes on both ends and a cathode in the middle, see Figure 2.3, for a photo of the HCL running with magnesium and neon, and Figure 2.4 for a schematic cross-section of the lamp. The cathode itself is about 4 cm long with an inner diameter about 8mm. It is made from the element of interest when possible, but otherwise a small piece of the element to be studied is placed inside or a powdered form is smeared on the wall of the cathode. The material of the glass window depends on the studied wavelength region. A sapphire window is transparent to the

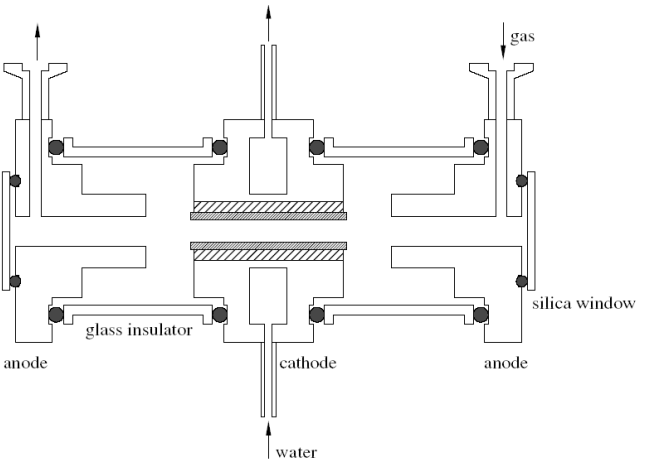

Figure 2.4: Cross-section of a hollow cathode lamp (Courtesy of U. Litzen).

infrared light which makes it useful when the measurements are performed in the infrared region whereas quartz is used for measurements in the ultraviolet region. The lamp is water-cooled to reduce the heating of the cathode.

Before measurements, the system is evacuated. The lamp is filled with a carrier gas, argon or neon in the present projects, with a pressure of $0.3 - 1.0$ Torr ($0.4 - 1.3$ mbar). The best working pressure depends on the carrier gas as well as the element of interest. When a voltage is applied, free electrons are accelerated and collide with the carrier gas atoms which get ionised. The ions are accelerated towards the cathode and hit the inner walls of the cathode and the sample of the element placed in the cathode. These collisions release atoms from the cathode material and the sample element to the plasma. This mechanism is called sputtering. The released atoms in the plasma are not only excited by collisions, mostly with electrons, but also through charge transfer with the carrier gas ions (Johansson & Litzen 1978, 1980).

In this thesis, different measurements have been performed with varying applied currents, usually between 0.1 A and 1.0 A. Increasing the applied current increases the number density in the plasma. This, in turn, increases the intensity of emission lines, see Figure 2.5. Although a high-current helps weak lines to be visible, it may cause a self-absorption effect on the strongest lines. This is a reabsorption of the same transition in another atom of the same species and is a radiative transfer ef-

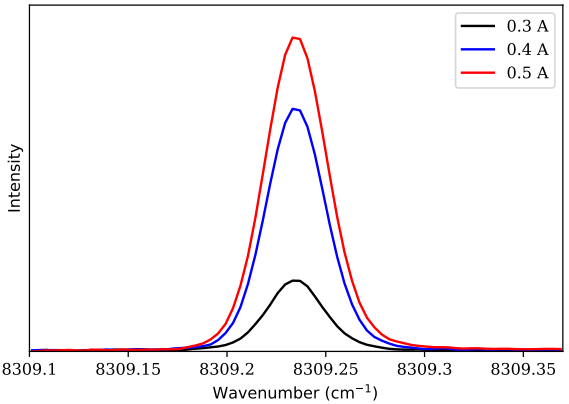

Figure 2.5: Illustration of the change in the line intensity with different applied current for the Si I 3p4s $^3P_2 - 3p4p\ ^3D_3$ line at 8309.24 cm^{-1}.

fect. Section 2.3 describes what a self-absorption effect is and how to correct for it.

Due to the design of the HCL, lines seen in the spectra are from neutral and singly ionised atoms which belong to the element of interest, the carrier gas, and the cathode material. The carrier gas lines can be used for wavenumber calibration as described in Section 2.4.1.

The HCL in Lund has been used for all of the projects but for Sc II measurements. For the Sc II project, measurements have been performed with a HCL at Imperial College, that is based on the Lund HCL design.

2.1.2 The Fourier transform spectrometer

Two different high-resolution Fourier transform spectrometers (FTSs) have been used to record the spectra analysed in the projects of this thesis: HR-IFS125 Bruker at the Lund Observatory (Edlén Laboratory) operating in the optical and infrared regions and Chelsea Instrument FT500 at the Imperial College (Blackett Laboratory) operating in the optical and UV regions.

The Lund instrument covers the wavenumber range of $50\,000 - 2000$ cm^{-1} ($200 - 5000$ nm) and has the maximum resolving power of $R = \sigma/\Delta\sigma = 10^6$ at 2000 cm^{-1}. Due to the insensitivity of the optical elements in the instru-

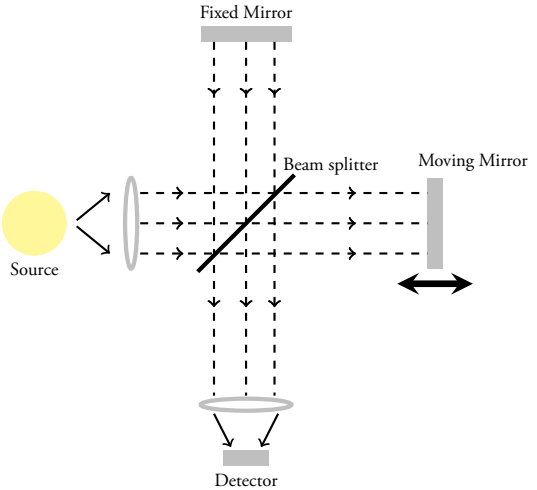

Figure 2.6: Illustration of an FTS based on the Michelson interferometer.

ment, such as mirrors, to higher wavenumbers, only the wavenumber region up to 20 000 cm^{-1} has been recorded using a resolution of 0.02 cm^{-1} in Paper I and IV, and 0.01 cm^{-1} in Paper II. The Imperial College instrument covers the wavenumber range 71 500 − 8700 cm^{-1} (140 − 1150 nm) and has the maximum resolving power of $R = 2{\cdot}10^6$ at 50 000 cm^{-1}. In Paper III, measurements have been performed with this instrument in the wavenumber region 23 500 to 63 100 cm^{-1} and using a resolution of 0.039 cm^{-1}.

The dominant broadening mechanism of spectral lines in a HCL is the Doppler broadening due to the thermal motions of the atoms. Doppler broadening has a full width at half maximum, FWHM, per wavelength/wavenumber of,

$$\frac{\Delta\lambda}{\lambda} = \frac{\Delta\sigma}{\sigma} = 7.16 \times 10^{-7}\sqrt{\frac{T}{M}} \tag{2.5}$$

where T is the ion temperature and M is the atomic mass number of the species. With a temperature around 2000K and the atomic mass of 21 as in the case for Sc I, the required resolving power ($\lambda/\Delta\lambda$) is 145 000 to resolve the Doppler broadening. The effect of the instrument function on the recorded line shape and width is negligible, if the resolving power is a factor of two or three greater than the required power derived from Doppler broadening (Thorne 1987).

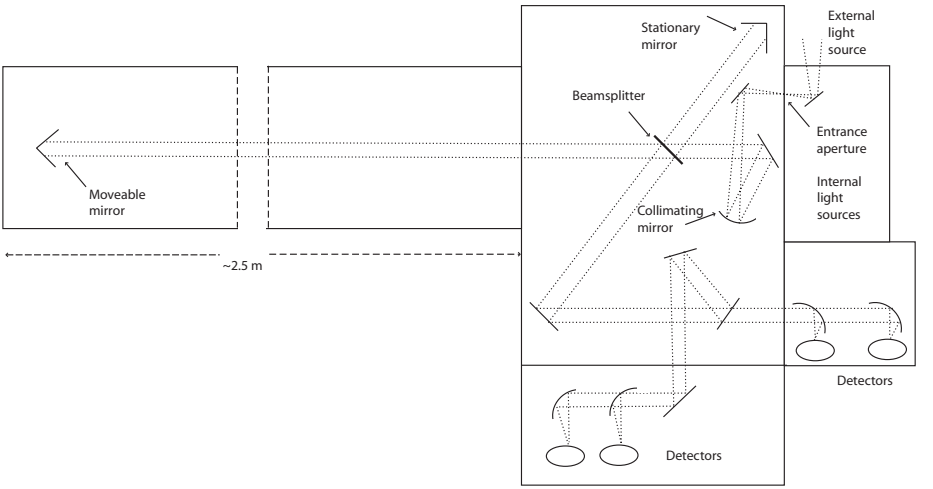

Figure 2.7: Schematic figure of the Bruker IFS 125 HR infrared FTS (Courtesy of G. Ljung).

An FTS is based on the Michelson Interferometer concept which is illustrated in Figure 2.6. The light beam from the source, S, splits into two beams at the beam splitter. Half of the beam goes through the beam splitter and is reflected from the moving mirror. The other half is reflected from the beam splitter, goes to the fixed mirror and reflected back from the fixed mirror. The two beams recombine at the beamsplitter and are registered at the detector. Since one of the mirrors moves along the axis of the beam, the path lengths will be different for the two beams and be varied throughout the movement. The recorded intensity at the detector as a function of the optical path difference can be written as,

$$I(x) = \int_{-\infty}^{\infty} B(\sigma)\cos(2\pi\sigma x)d\sigma \tag{2.6}$$

where x is the path difference between the two beams, $B(\sigma)$ is the spectral distribution of the incoming light and σ is the wavenumber (Thorne et al. 1999; Davis et al. 2001). This recorded intensity as a function of path difference is called an interferogram which is a Fourier transform of a spectrum. Therefore, taking an inverse Fourier transform of an interferogram will give a spectrum,

$$B(\sigma) = \int_{-\infty}^{\infty} I(x)\cos(2\pi\sigma x)dx. \tag{2.7}$$

This transformation has been performed either by the computer programme OPUS supplied by the BRUKER company and used for the measurements at Lund Observatory or with the computer software XGREMLIN (Nave et al. 2015) for the measurements carried out at Imperial College.

The FTS concept is based on a Michelson interferometer but with more sophisticated set-up, see Figure 2.7 for a drawing on the Lund Observatory HR-IFS125 Bruker instrument. Before any measurements, the instrument is evacuated to avoid turbulences and vibrations, and molecules in the instrument. The HeNe laser in the instrument traces the mirror movement, thus the path difference, and gives a multiplicative wavenumber scale. However, the finite aperture size and the non-parallel alignment of the incoming beam and the laser beam may affect the wavenumber scale (Learner & Thorne 1988). This can be corrected by a wavenumber calibration as described in Section 2.4.1.

In addition to the high wavenumber accuracy derived from the HeNe laser, an FTS has two more advantages: multiplexing and large throughput (Svanberg 2001). The former means that an FTS can record a spectrum at all wavelengths simultaneously. This, in turn, implies a shorter measurement time compared to scans for one wavelength at a time, such as diffraction gratings. The radius of the collimation mirror (the first optical element) determines the amount of throughput. A large radius means a large throughput, $throughput \propto r^2$, which in turn allows more light reach to the detector. A drawback with multiplexing is the noise level, since the noise from strong features is distributed on all wavelength regions. Using filters is thus an important tool to increase the signal-to-noise ratio.

2.1.3 Experimental set-up and other equipments

The experimental set-up used during the measurements is shown in Figure 2.8. Light from the HCL enters to the FTS through the aperture with the help of a folding mirror. It goes through a filter and reaches the detector. It is important to have all these components aligned for two reasons: i) to make maximum amount of the photons reach to the detector, ii) to make photons from different sources have the same optical path. Misaligned components may affect the results.

In addition to the HCL light source, a calibration lamp is placed at the same distance as the HCL to the FTS. A folding mirror helps changing between light sources, either the HCL or the calibration lamp, without moving the lamps. The

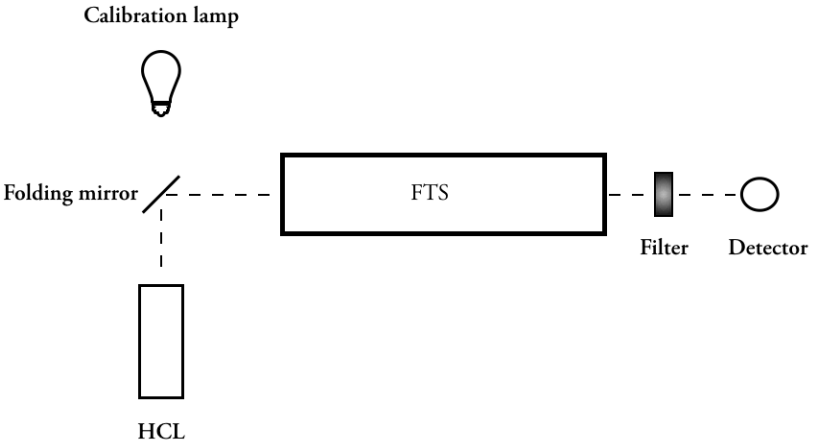

Figure 2.8: Experimental set-up for branching fraction measurements.

calibration lamp has two roles: to control if anything has changed between different measurements and to help determining the response function of the instrument. Its spectra are taken before and after every HCL lamp recording, and in this way one can confirm the response function does not change during the measurements. To determine the intrinsic relative intensity of the spectral lines, one should know the response function which is the wavelength dependent transmission of the optical components and detector of the instrument. It can be determined from the true radiance and the observed spectrum of the calibration lamp. This calibration procedure is described in Section 2.4.2 in detail. In this thesis projects, tungsten lamps and a deuterium lamp have been used along with a blackbody emitter with known temperature. One of the tungsten lamps has been calibrated by the Swedish National Laboratory (SP) for the range $40\,000 - 4000$ cm^{-1} ($250 - 2500$ nm) and has been used in Paper I, II, and IV. The other tungsten lamp was calibrated by the UK National Physical Laboratory for the $33\,000 - 12\,500$ cm^{-1} ($300 - 800$ nm) wavenumber region which has been used in Paper III. The deuterium lamp has been calibrated by Physikalisch-Technische Bundesanstalt (PTB), in Berlin for the spectral region $86\,200 - 24\,390$ cm^{-1} ($116 - 410$ nm).

The spectra have been recorded with different detectors and filters sensitive to photons in the wavelength region of interest. This helps to reduce the noise as light

from other regions is blocked. Noise can have different sources, the dominating ones are the photon noise and the detector noise (Thorne et al. 1999; Davis et al. 2001). In the optical and UV region, the noise usually arises from the photon noise and this can be reduced by using filters and detectors only sensitive to a specific wavelength region. In the IR region, in addition to the photon noise, there is the detector noise. The noise level can be decreased by using detectors sensitive to this region and by cooling. In the measurements out to 2000 cm^{-1}, we observe that the blackbody radiation of the hollow cathode contributes to the noise of the measured spectrum. In Paper I, II, and IV, we have used an indium antimonide (InSb) detector sensitive to the photons in the wavenumber region $1850 - 11\,000$ cm^{-1}, an indium gallium arsenide (InGaAs) detector sensitive to the photons between 6000 and 15 000 cm^{-1}, a silicon (Si) detector sensitive to the photons between 8000 and 21 000 cm^{-1}, and a photomultiplier tube (PMT) detector sensitive to the photons in the wavelength region $12\,000 - 21\,000$ cm^{-1}. In Paper III, we have used two different PMT detectors sensitive to $23\,700 - 47\,400$ cm^{-1} and $31\,500 - 63\,000$ cm^{-1} regions.

Moreover, molecules in the humid air, such as water and carbon-dioxide, have absorption bands in the infrared wavelength region. Those bands are visible on spectra of the calibration lamp, and thus affect the observed spectra of the species studied in this thesis. For this reason, we isolated a part of the experimental set-up, where the calibration lamp and the HCL are, and placed liquid nitrogen to trap the molecules. This set-up reduced the amount of molecules and hence the absorption from them.

2.2 Lifetime measurements with TR-LIF method

Lifetime measurements are complementary to BF measurements, because the transition probability of a line is derived as the ratio between the BF of the line and the lifetime of the upper level. In Paper III, reported radiative lifetimes have been measured with the two-step Time-Resolved Laser Induced Fluorescence (TR-LIF) method at the Lund High Power Laser Facility. The two-step excitation method allows to excite the levels that are not directly possible to reach from the ground level, such as the highly excited levels which would require lasers with short wavelengths or the levels with the same parity as the ground or lower excitation states. The latter cannot be excited from the lower levels since the excitation is not possible with a E1 transition and must be through a M1 or E2 transition.

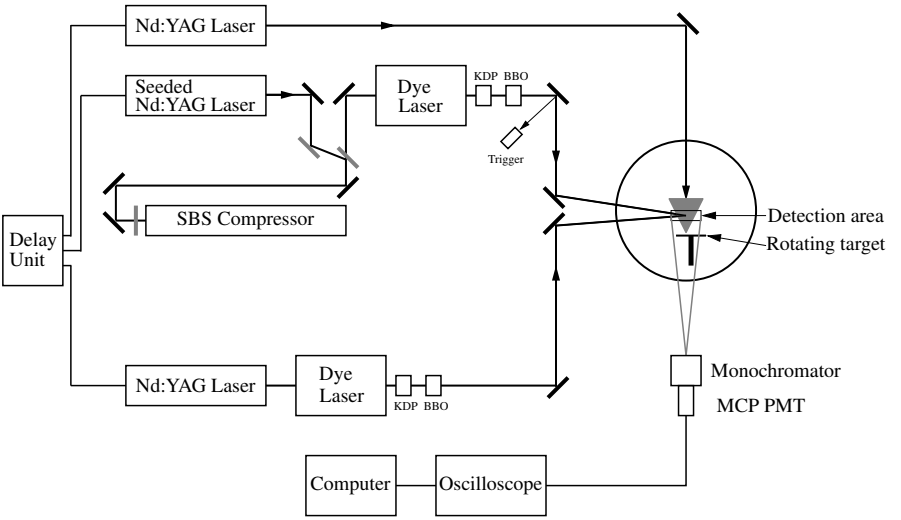

Figure 2.9: Lifetime measurements set-up at the Lund High Power Laser Facility with two-step excitation.

The transition probability is then much lower compared to the allowed transitions.

The experimental set-up, used in Paper III, is illustrated in Figure 2.9. A solid piece of the target element is placed on a rotating plate just below the detection area and laser pulses (from the top laser in the figure) are directed perpendicular to the target to produce the plasma with the free atoms and ions targeted in the measurements. Two additional lasers (middle and bottom lasers) are responsible for the two-step excitation. The laser light is tuned to match the desired excitation wavelength. In other words, the laser light wavelength is adjusted to populate the intermediate level or the final level. In cases when a shorter wavelength (or higher frequency) than the wavelength that can be achieved with the dye lasers is needed to reach the desired levels, KDP and BBO crystals are used to double or triple the frequency, respectively.

The lifetimes in Paper III are in the range $1.09 - 3.80$ ns, whereas the pulses from the excitation lasers have widths of 10 ns. The laser pulses are thus too long to be able to measure the interesting levels. To shorten the laser pulses of the sec-

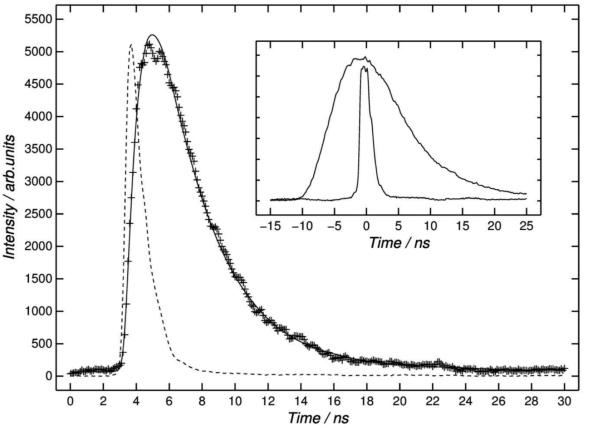

Figure 2.10: Example of a recorded decay (+) that is a convolution of the second step excitation laser pulse (dashed line) and the single exponential decay of the excited level. The solid line shows the fitted convolution curve. The small figure shows the delay between the first step laser pulse (broad curve) and the second laser pulse (narrow curve) (Lundberg et al. 2016).

ond excitation laser (middle one in the figure), a stimulated Brillouin scattering (SBS) cell is applied. This is a water cell which temporally compresses the laser pulse to widths around 1 ns making shorten lifetimes accessible.

The timing between the ablation laser pulse producing the plasma, the first excitation pulse, and finally the second step excitation pulse is crucial. The delay unit controls not only the timing between the plasma generating laser and the first step excitation laser but also the delay between the first and second step excitation lasers. The first delay is used to time the measurements to parts of the plasma where the plasma conditions are optimal, such as recombination background and atom dynamics. The latter delay is to time the second step laser pulses to a time when the population of the intermediate level is at its maximum and not varying, as seen in Figure 2.10.

The fluorescence signal from the final level is filtered out with a grating monochromator and recorded by a photomultiplier tube detector. The recorded signal is a convolution of the second step excitation laser pulse and the exponential decay of the excited level, see Figure 2.10. Because of this reason, the laser pulse and

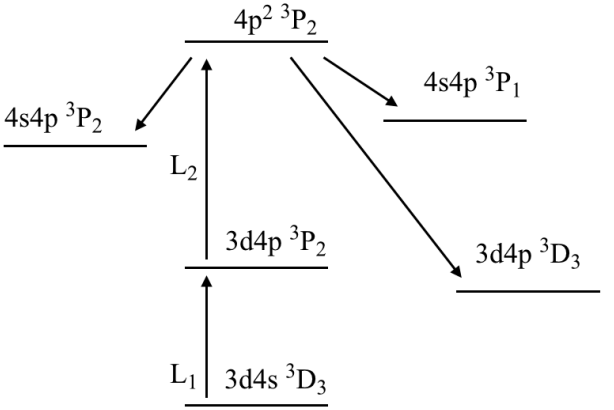

Figure 2.11: Example of a two step excitation from the ground state 3d4s $^3D_3$ to 4p^2 $^3P_2$ in Sc II.

fluorescence signal are recorded simultaneously for each measurements. By fitting a convolution curve, one can determine the lifetime of the excited level. Studies of complex spectra with many levels and lines, such as Sc II, requires a tuneable and narrow-line excitation laser to ensure that only one level is excited at a time which makes the blending less problematic. Despite this fact, the dense level structure makes blending an issue. A careful analysis of the lines in both the excitation channel and the fluorescence is needed. When utilising a two-step excitation scheme, as in the present study, blending by decays from intermediate level decays, or cascade decays from the level studied is a possibility. Analyses of several decay channels of the same levels are used when possible.

Figure 2.11 shows an example of a two-step excitation measurement. After the ablation laser has created the plasma, the first step excitation laser populates the intermediate level 3d4p $^3P_2$ from the ground level 3d4s $^3D_3$. The second step laser excites the atom from the intermediate level to the final level 4p^2 $^3P_2$. The decay signal has been observed in three channels from decays to 4s4p $^3P_2$, $^3P_1$, and $^3D_3$ levels.

2.3 Self-absorption analysis

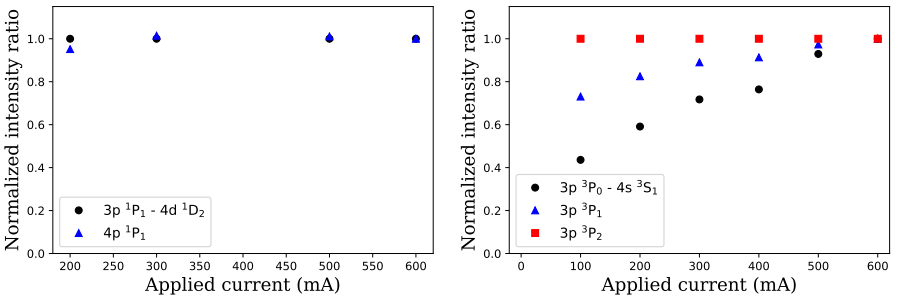

(a) (b)

Figure 2.12: Self-absorption test for Mg I lines. a) Intensity ratios of the lines from the upper level $4d^1D_2$ shows no change as a function of the applied discharge current. This indicates that the lines are self-absorption free. b)Intensity ratios of the lines from the upper level $4s^3S_1$ decreases as the applied discharge current decreases. This clearly indicates the presence of self-absorption.

An emitted photon from one atom might be absorbed by another atom of the same element before it escapes from the plasma; this is known as self-absorption. The probability of self-absorption depends on the physical dimensions of the plasma and the absorption coefficient which in turn depends on the transition strength and the density of the plasma (Kunze 2009; Gray 2005).

The self-absorption reduces the intensity of a line, therefore the observed intensity will be too low compared to the true intensity. This, in turn, will affect the BFs and the derived oscillator strengths will be incorrect. In the spectroscopic experiments, it is important, often needed, to apply high discharge current as it helps improving the signal-to-noise ratio (SNR) by increasing the number density in the plasma. However, this increases the effect of self-absorption, too. In addition, transitions to the ground level or to the metastable levels are more likely to be affected by self-absorption due to the high population of the lower levels of these transitions.

Different plasma conditions cause different amount of self-absorption. To investigate self-absorption effects, the measurements are carried out with different applied disharge currents. These effects are determined by studying the intensity

ratios of the lines from the same upper level as a function of the applied current. If the ratio does not change, it means there is no self-absorption. However, if the ratio varies systematically with the current, this indicates the presence of self-absorption. The self-absorption effects can be compensated by correcting the line intensities or line ratios. This is done by extrapolating a line ratio to the ratio at zero current, where the true line ratio is assumed to be not affected by self-absorption. This method was tested by Sikström et al. (2002) where their extrapolated zero current Fe I line ratios agreed very well with the Blackwell et al. (1979) absorption measurement values.

Figure 2.12 shows an example of normalised intensity ratios plotted as a function

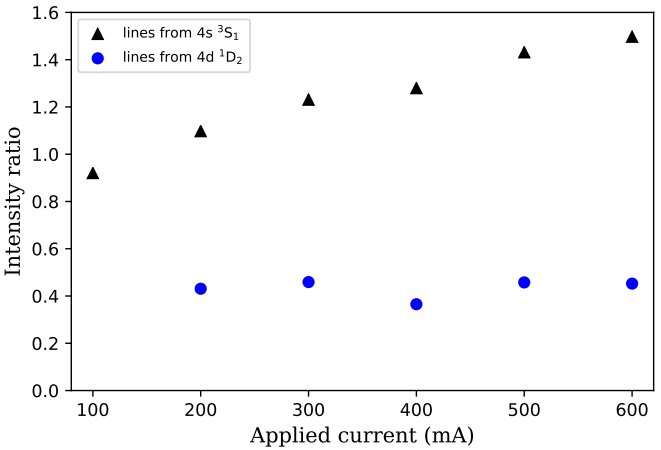

Figure 2.13: Alternative example of a self-absorption test for the same lines as in Figure 2.12. The intensity ratio is between the sum of the intensities from the weaker lines and the intensity of the strongest line from the same upper level. Note that the lines from the 4d $^1D_2$ level are not strong enough to be measured with 100 mA.

of applied currents for Mg I lines. In Figure 2.12a, the normalised intensity ratios of 3p $^1P_1$ - 4d $^1D_2$ and 4p $^1P_1$ - 4d $^1D_2$ lines do not show any change with increasing current, and thus these lines are not affected by self-absorption. On the other hand, Figure 2.12b shows the normalised intensity ratios of the transitions from the $4s^3S_1$ level and it is clear that the ratios change with increasing intensity. This plot implies that the lines are affected by self-absorption. Alternatively, one can plot the intensity ratios as the sum of intensities of the weaker lines from the

same upper level divided by the strongest line intensity from the same upper level, as seen in Figure 2.13 for the same lines as in the previous example. In this plot, the change in the intensity ratio indicates that the strongest line is affected by self-absorption. To correct this effect, a line has been extrapolated to the zero current value. The uncertainty of the fit has been included in the total uncertainty of the line intensities. The zero current value (intercept) has been used in the derivation of the BF, and is then corrected for the self-absorption effect on the strongest line.

2.4 Calibration

2.4.1 Wavenumber calibration

The HeNe laser in the FTS keeps track of the mirror movement in the instrument and gives a linear wavenumber scale to the recorded spectrum. The accuracy of the wavenumbers is usually enough to identify lines. However, for a higher accuracy one has to calibrate the wavenumbers. The shift in the wavenumber arises from two reasons: the finite size aperture and the imperfect alignment of the laser beam and the incoming light beam (Learner & Thorne 1988; Salit et al. 1996). It can be calibrated with a correction factor,

$$\sigma_{\text{true}} = (1 + k_{\text{eff}})\sigma_{\text{apparent}} \tag{2.8}$$

where σ_{true} is the true wavenumber, k_{eff} is the correction factor, and σ_{apparent} is the measured wavenumber (Davis et al. 2001). Usually, the correction factor is obtained by an internal light wavenumber standard, such as the carrier gas lines produced in the HCL. One of the advantages of using the internal gas lines for wavelength calibration is the same optical path which does not introduce further uncertainties. In principle, it is enough to use only one line to put the wavenumbers on an absolute scale (Learner & Thorne 1988), nevertheless using many lines will help to improve the accuracy and to avoid systematic errors. The correction factor of a line i is derived from Eq. 2.8,

$$k_{\text{eff},i} = \frac{\sigma_{\text{true},i}}{\sigma_{\text{apparent},i}} - 1. \tag{2.9}$$

For n different calibration lines, the correction factor can be determined from the mean of all correction factors weighted by the inverse variance,

$$k_{\text{eff}} = \frac{\sum_{i=1}^{n} k_{\text{eff},i}\, u^{-2}(k_{\text{eff},i})}{\sum_{i=1}^{n} u^{-2}(k_{\text{eff},i})} \tag{2.10}$$

where $u(k_{\text{eff},i})$ is the uncertainty in the correction factor which is determined from the propagation of errors,

$$\frac{u^2(k_{\text{eff},i})}{(k_{\text{eff},i}+1)^2} = \left(\frac{u^2(\sigma_{\text{true},i})}{\sigma^2_{\text{true},i}} + \frac{u^2(\sigma_{\text{apparent},i})}{\sigma^2_{\text{apparent},i}} \right). \tag{2.11}$$

In Paper II, the correction factor has been determined with Ar I lines. Eq. 2.8 has been applied to obtain the true wavenumbers of Sc II lines. Ar II lines were too weak to calibrate the lines in the wavenumber region of interest. When calibrated, the total uncertainty in the wavenumber is the combination of the uncertainty in the observed central position of each line and the uncertainty in the correction factor,

$$\frac{u^2(\sigma)}{\sigma^2} = \left(\frac{u^2(\sigma_{\text{obs}})}{\sigma^2_{\text{obs}}} + \frac{u^2(k_{\text{eff}})}{(1+k_{\text{eff}})^2} \right). \tag{2.12}$$

The typical total wavenumber uncertainty is usually very small ~ 0.001 cm^{-1}.

2.4.2 Intensity calibration

To determine the true relative intensities, one should calibrate for the response of the instrument. All optical elements in the FTS contribute to the instrument response. This can be compensated by measuring a spectrum of a reference light source with a known radiance, using the same experimental setup and the equivalent optical path. In Paper I, II, and IV, a tungsten filament lamp has been used as a reference light. This lamp has been calibrated in the range $40\,000 - 4000$ cm^{-1} ($250 - 2500$ nm). In addition to that, in Paper II and IV, a blackbody lamp has been used to extend the calibration to longer wavelengths ($\lambda > 2500$ nm). In Paper III both a tungsten filament lamp and a deuterium lamp have been used since the experiments were performed between $23\,500 - 63\,100$ cm^{-1} ($425 - 158$ nm). The deuterium lamp has some emission structure on its continuum, therefore the measured deuterium lamp spectrum has been binned to match the reference data.

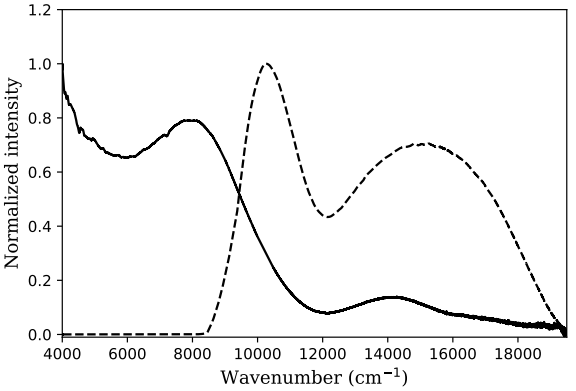

Figure 2.14: Response functions of the instrument normalised to the peak of each curve. The dashed line was acquired with the Si detector and the solid line with the InSb detector.

The calibration procedure starts with recording the spectrum of the calibration lamp with the same optical set-up and conditions as the BF measurements. Dividing the recorded calibration lamp spectrum with the known spectral radiance will give the response of the instrument for the specific set-up. Figure 2.14 shows the resulting response functions of the Bruker IFS 125 HR instrument at Lund Observatory obtained for different detectors, namely the InSb and the Si. In cases where lines from the same upper level are at different wavelength region, the lines in the overlapping region of the detectors can be used to connect the relative intensities of the two wavelength regions.

Another example is shown in Figure 2.15. The left figure shows the partial radiances of the tungsten and the deuterium lamps in the region $23\,000 - 39\,000$ cm^{-1} and the right figure shows the response functions derived from the two lamps radiances and observed spectra. In Paper III, we have measured Sc II lines in the region where both of the calibration lamps were needed to cover the full region. Therefore, the spectra of the lamps have been recorded one after the other for the same experimental set-up. The overlapping wavenumber region is $24\,390 - 33300$ cm^{-1}. As seen in Figure 2.15b, the acquired normalised response functions from the two lamps are very similar, as expected. In this way, the full wavenumber range needed for the intensity calibration of the Sc II lines

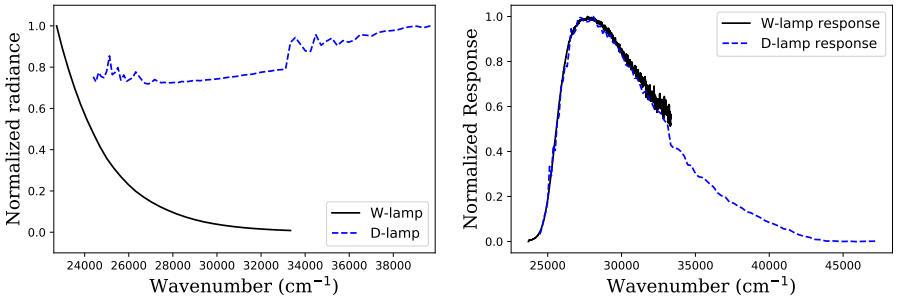

(a) (b)

Figure 2.15: a) Partial radiances of the tungsten lamp and the deuterium in the region 24 390 − 33 300 cm^{-1}. b) Response functions of the instrument determined from the tungsten lamp and the deuterium lamp.

has been covered. In addition, this figure indicates that the systematic errors are very small.

2.5 Oscillator strengths

Oscillator strengths, f-values, in the projects of this thesis have been obtained from BFs and radiative lifetimes. The BFs have been measured either with the Lund FTS or London FTS using a HCL as a light source. Moreover, the radiative lifetimes have been measured with a two-step TR-LIF method at Lund High Power Facility when possible (Paper III), taken from measurements in the literature (Paper I and II) or calculated using the atomic structure codes ATSP2K and GRASP2K (Paper II and IV).

After correcting the relative line intensities for instrument response function and self-absorption, the BFs have been obtained from,

$$(BF)_{\mathrm{ul}} = \frac{A_{\mathrm{ul}}}{\sum_i A_{\mathrm{u}i}} = \frac{I_{\mathrm{ul}}}{\sum_i I_{\mathrm{u}i}}. \tag{2.13}$$

The latter equality follows from the fact that all the lines decay from the same upper level and the intensity of a transition is proportional to the transition probability of that transition, the statistical weight of the upper level, and the population of the upper level, therefore BFs can be determined as relative intensity ratios.

Combining BFs with radiative lifetimes, transition probabilities have been determined from,

$$A_{\rm ul} = \frac{BF_{\rm ul}}{\tau_{\rm u}}. \tag{2.14}$$

Finally, using Eq. 2.1, f-values have been derived from,

$$f = \frac{g_{\rm u}}{g_{\rm l}} \lambda^2 A_{\rm ul} 1.499 \times 10^{-16}, \tag{2.15}$$

where $g_{\rm u}$ and $g_{\rm l}$ are the statistical weights of the upper and lower level, respectively, λ is in Å and $A_{\rm ul}$ is in $\rm s^{-1}$.

2.6 Uncertainties

The uncertainty in the transition probability and therefore in the f-value includes the uncertainty in the upper level lifetime, $\tau_{\rm u}$, and the uncertainty in the BF. From the propagation of errors, the relative uncertainty is,

$$\left(\frac{u(f)}{f}\right)^2 = \left(\frac{u(A)}{A}\right)^2 = \left(\frac{u(BF)}{BF}\right)^2 + \left(\frac{u(\tau)}{\tau}\right)^2. \tag{2.16}$$

The main contribution to the uncertainty in the experimental $\tau_{\rm u}$ is usually the variation between measurements, since the statistical uncertainties from the fitted lifetimes are very low (Palmeri et al. 2008) compared to the day-to-day variations. The uncertainty in the BF further contains the uncertainty in the measurement of line intensity, uncertainty in the calibration lamp, and uncertainty in the normalisation factor that connects different spectral regions if different detectors are used. The uncertainty in the intensity includes the uncertainty of the self-absorption correction. The uncertainty of the calibration lamp includes the calibration uncertainty and the variation between the repeated calibration lamp measurements. The final total uncertainties have been derived from the methods described in Sik-

ström et al. (2002) assuming the contributions are uncorrelated,

$$\left(\frac{u(A_k)}{A_k}\right)^2 = (1-(BF)_k)^2\left(\frac{u(I_k)}{I_k}\right)^2 + \sum_{j\neq k(\text{in P})}(BF)_j^2\left(\left(\frac{u(I_j)}{I_j}\right)^2+\left(\frac{u(c_j)}{c_j}\right)^2\right) + \sum_{j\neq k(\text{in Q})}(BF)_j^2\left(\left(\frac{u(I_j)}{I_j}\right)^2+\left(\frac{u(c_j)}{c_j}\right)^2+\left(\frac{u(nf)}{nf}\right)^2\right) + \left(\frac{u(\tau)}{\tau}\right)^2, \tag{2.17}$$

where $u(I_k)$ is the uncertainty of the line intensity including the uncertainty of self-absorption correction, $u(c)$ is the uncertainty in the calibration lamp and $u(nf)$ is the uncertainty in the normalisation factor. The second line of the equation includes the intensity uncertainties of other lines from the same upper level detected within the spectral region of the same detector P, and the third line includes the intensity uncertainties of other lines from the same upper level detected with detector Q.

In addition, all the lines from the same upper level may not be visible due to the low transition probability. In these cases their residuals are determined from calculations (usually $< 10\%$) and the relative uncertainty of these lines has been estimated to 50% and added in the uncertainty budget.

In the projects of this thesis, the relative uncertainties of the f-values are between 5% for the strong lines and 25% for the weak lines or for the lines with high uncertainty in their radiative lifetime.

Chapter 3

Calculations of oscillator strengths

In order to calculate atomic data, such as oscillator strengths, between the lowest states of an N-electron system, the corresponding wavefunctions, $\Psi(\boldsymbol{q}_1, \ldots, \boldsymbol{q}_N)$, where $\boldsymbol{q} = (\boldsymbol{r}, \sigma)$ represents both the space and spin coordinates of an electron, should be known. The wavefunctions are solutions to the time-independent Schrödinger equation,

$$\mathcal{H}\Psi(\boldsymbol{q}_1, \boldsymbol{q}_2, \ldots, \boldsymbol{q}_N) = E\Psi(\boldsymbol{q}_1, \boldsymbol{q}_2, \ldots, \boldsymbol{q}_N), \tag{3.1}$$

where the Hamiltonian operator, $\mathcal{H}$, depends on the quantum mechanical formalism; a relativistic system or a non-relativistic system. It is convenient to use atomic units here on, where the unit of length is defined by the Bohr radius, $a_0 = 4\pi\varepsilon_0\hbar^2/me^2$, the unit of mass is the rest-mass of the electron, the unit of charge is set to the magnitude of the electron charge, and the angular momentum $\hbar$, is equal to unity (Hartree 1957). A non-relativistic $\mathcal{H}$ in atomic units is defined as,

$$\mathcal{H} = \sum_{i=1}^{N}\left(-\frac{1}{2}\nabla_i^2 - \frac{Z}{r_i}\right) + \sum_{i>j}^{N}\frac{1}{r_{ij}}, \tag{3.2}$$

where Z is the nuclear charge, r_i is the distance from the nucleus and r_{ij} is the distance between two electrons. The first term is the kinetic energy, the second term arises from the potential energy of the electrons and the third one accounts for the interaction between the electrons.

During calculations we need to keep in mind the properties of the wavefunctions as described in Froese Fischer et al. (1997):

- The wavefunctions belonging to the discrete spectrum part of the Hamiltonian represent bound states. These wavefunctions are square integrable and can be normalised.
- Electrons are indistinguishable, therefore the wavefunctions should be antisymmetric.
- The non-relativistic Hamiltonian commutes with the squares and projections of the total orbital and spin angular momentum operators. Therefore, the wavefunction should be simultaneous eigenfunctions to all $\mathcal{H}$, $\mathbf{L}^2$, L_z, $\mathbf{S}^2$, S_z. The eigenvalues of these operators are E, $L(L+1)$, M_L, $S(S+1)$, and M_s, respectively and the wavefunction is labelled by the angular momentum quantum numbers, L, M_L, S, and M_S.
- The wavefunction should be an eigenfunction to the parity operator, Π, as the parity operator commutes with the angular momentum operators and the Hamiltonian operator.

Although, Eq. 3.1 seems to be easy to solve, it is computationally challenging and some approximations are needed. Hartree (1957) explained the necessity of approximations in atomic structure calculations with an example. In this thesis case, if we consider Mg I with 12 electrons, each electron has its own 3D-space, therefore there will be $12 \times 3 = 36$ space variables. If we want to numerically represent the wavefunction by giving the function values on a grid with ten values (which is still very modest), in each space dimension we will need 10^{36} values. This is impossible to handle even with supercomputers. This example shows the need for approximations in atomic structure calculations for systems with more than four electrons. Approximate solutions to Eq. 3.1 for many electron systems are all constructed from one electron solutions.

3.1 One-electron solution

The Schrödinger equation in spherical coordinates and in a general spherical potential $U(r)$ for one-electron system is (Hartree 1957),

$$\mathcal{H}\phi(r,\theta,\varphi,\sigma) = E\phi(r,\theta,\varphi,\sigma), \tag{3.3}$$

where the Hamiltonian in atomic units is,

$$\mathcal{H} = -\frac{1}{2}\left(\frac{1}{r^2}\frac{\partial}{\partial r}\left(r^2\frac{\partial}{\partial r}\right) + \frac{1}{r^2\sin\theta}\frac{\partial}{\partial\theta}\left(\sin\theta\frac{\partial}{\partial\theta}\right) + \frac{1}{r^2\sin^2\theta}\frac{\partial^2}{\partial\varphi^2}\right) + U(r). \tag{3.4}$$

$U(r) = -Z/r + V(r)$ and $V(r)$ is the central potential. This Schrödinger equation can be solved by the separation of variables method and the solutions are of the form of

$$\phi(r, \theta, \varphi, \sigma) = \left(\frac{1}{r}\right) P(r) Y(\theta, \varphi) \chi_{m_s}(\sigma). \tag{3.5}$$

The angular equation becomes,

$$\frac{1}{\sin\theta}\frac{\partial}{\partial\theta}\left(\sin\theta\frac{\partial Y}{\partial\theta}\right) + \frac{1}{\sin^2\theta}\frac{\partial^2 Y}{\partial\varphi^2} + \lambda Y = 0 \tag{3.6}$$

where $\lambda = l(l+1)$ with $l = 0, 1 \ldots$. Y are the spherical harmonics that are eigenfunctions to both the orbital angular momentum operator and the parity operator, and characterised by l and m. This part is simple enough to solve and the derivations can be found in many text books (see for example Pradhan & Sultana 2011). The radial part is more complicated to solve. Bound state solutions to

$$\left(\frac{\mathrm{d}^2}{\mathrm{d}r^2} - 2U(r) - \frac{l(l+1)}{r^2} + 2E\right) P(r) = 0 \tag{3.7}$$

should satisfy the boundary conditions $P(0) = 0$ and $P(\infty) = 0$, and $P(r)$ must be normalised. Such solutions can be found only for certain discrete energy values, E, and they depend on the principal quantum number, n, and the orbital quantum number, l. Derivations of analytical and numerical solutions can be found in Cowan (1981). The one-electron wavefunctions can be written as,

$$\phi(r, \theta, \varphi, \sigma) = \left(\frac{1}{r}\right) P(nl; r) Y_{lm_l}(\theta, \varphi) \chi_{m_s}(\sigma), \tag{3.8}$$

and are known as spin-orbitals.

3.2 Variational method

For many-electron systems, we need approximate methods to determine wavefunctions. These methods usually rely on the variational method. Determining a normalised solution to Eq. 3.1 is equivalent to determining a function Ψ that leaves the functional,

$$\mathcal{F}(\Psi) = \langle\Psi|\mathcal{H}|\Psi\rangle + \lambda\langle\Psi|\Psi\rangle, \tag{3.9}$$

stationary to first order with respect to all variations, $\delta\Psi$, in Ψ. λ is a so called Lagrange multiplier and is determined such that the normalisation condition,

$\langle\Psi|\Psi\rangle = 1$ is fulfilled (Froese Fischer et al. 1997).

In practise, the variational problem can not be solved exactly. Instead, we choose a variational function Ψ_v that depends on a various parameters, $\boldsymbol{\alpha} = (\boldsymbol{\alpha}_1, ..., \boldsymbol{\alpha}_n)$

$$\Psi_v = \Psi_v(\boldsymbol{\alpha}; \boldsymbol{q}_1, ..., \boldsymbol{q}_N). \tag{3.10}$$

Then these parameters are determined from the stationary condition of the functional, $\mathcal{F}(\boldsymbol{\alpha}) = \langle\Psi_v|\mathcal{H}|\Psi_v\rangle + \lambda\langle\Psi_v|\Psi_v\rangle$, with respect to variations of the parameters,

$$\frac{\partial\mathcal{F}(\boldsymbol{\alpha})}{\partial\alpha_i} = 0 \quad i = 1, \ldots, n \tag{3.11}$$

with λ determined from the normalisation constraint, $\langle\Psi_v|\Psi_v\rangle = 1$ (Froese Fischer et al. 1997). This is a problem that can be solved on a computer. The variational function, Ψ_v, represents the best approximate solutions of the Eq. 3.1 within the function space spanned by the variational function. In addition, the variational function should have the same properties as the exact eigenfunction described in the beginning of this Chapter.

3.3 Hartree-Fock method

The simplest variational function, that has the correct qualitative features, is the Hartree-Fock wave function. In this method (Hartree 1928; Fock 1930a,b), the variational function is taken as a product of one-electron functions, or spin-orbitals. The product of one-electron functions is antisymmetrized and is a linear combination of antisymmetrized product functions with different combinations of m_l and m_s quantum numbers to form a function that is also an eigenfunction of $\mathbf{L}^2$, L_z, $\mathbf{S}^2$, S_z. Such a function is called a configuration state function (CSF), $\Phi(\gamma LS)$, where γ specifies the principal and orbital quantum numbers of the spin-orbitals used in the construction and in addition gives information on how the individual angular momenta are coupled together to give the final total angular momenta L and S.

Applying the variational principle with respect to the variations in the radial function, $P(nl; r)$ and using the energy functional,

$$\mathcal{F}(\ \mathbf{P}) = \mathcal{E}(\gamma LS) + \sum_{a\leqslant b} \delta_{l_a l_b} \lambda_{ab} \langle P(a; r)|P(b; r)\rangle \tag{3.12}$$

where a and b are the short notations for $n_a l_a$ and $n_b l_b$, one gets a set of coupled integrodifferential equations, known as the Hartree-Fock equations,

$$\left(\frac{\mathrm{d}^2}{\mathrm{d}r^2} + \frac{2}{r}[Z - Y(a;r)] - \frac{l_a(l_a+1)}{r^2} - \varepsilon_{aa}\right) P(a;r) = \frac{2}{r} X(a;r) + \sum_{\substack{b=1 \\ b\neq a}}^{m} \delta_{l_a l_b} \varepsilon_{ab} P(b;r). \tag{3.13}$$

for unknown radial functions. The quantities ε_{aa} and ε_{ab} are the diagonal and off-diagonal energy parameters, respectively, related to the Lagrange multipliers, λ_{ab}, introduced in the functional to preserve the orthogonality of the radial orbitals. The equations are coupled to each other through, $Y(a;r)$, the direct potential, that can be interpreted as a screening of the nucleus, and the exchange potential $X(a;r)$ that arises from the anti-symmetrisation of the variational function. The derivations of these equations can be found in the many text books (such as Cowan 1981; Froese Fischer et al. 1997).

The Hartree-Fock equations are solved iteratively in the so-called self-consistent field procedure: estimate the radial orbitals and solve the equations repeatedly until the radial functions do not change any more.

3.4 Multiconfiguration Hartree-Fock method

In the Hartree-Fock method, electrons move independently in the field of the nucleus and of the other electrons, however, in reality this is not the case. The method does not include the correlation in the motion of the electrons, hence electrons do not interact with each other. The solutions derived from the Hartree-Fock (HF) method are not the exact solutions of the Schrödinger equation. Because of this reason, Löwdin (1955) introduced the so-called correlation energy,

$$E^{\text{corr}} = E^{\text{exact}} - E^{HF}, \tag{3.14}$$

where the E^{exact} is the exact solution of the Schrödinger's equation. The HF method can be improved by the multiconfiguration Hartree-Fock method (MCHF) in which the electron correlation is taken into account and the total wavefunction

is assumed to be a linear combination of CSFs,

$$\Psi(\gamma LS) = \sum_{i=1}^{M} c_i \Phi(\gamma_i LS), \tag{3.15}$$

where c_i is called a mixing coefficient and $\sum_{i=1}^{M} c_i^2 = 1$ (Froese Fischer et al. 1997). Consequently, the problem expands to determining c_i coefficients and orbitals as an extension to the HF method (Froese Fischer et al. 2016). In this method, both c_i coefficients and radial parts of the spin-orbitals are varied for a stationary energy (Froese Fischer et al. 2016). The energy functional for this method becomes,

$$\mathcal{F}(\mathbf{P}, \mathbf{c}) = \varepsilon(\gamma LS) + \sum_{a \leqslant b} \delta_{l_a l_b} \lambda_{ab} \langle P(a;r) | P(b;r) \rangle - E \sum_{i=1}^{M} c_i^2. \tag{3.16}$$

For given radial functions, applying variations to the mixing coefficients leads to a matrix eigenvalue equation in the form of,

$$\mathbf{Hc} = E\mathbf{c}, \tag{3.17}$$

where $\mathbf{H}$ is a matrix with matrix elements given by $\langle \Phi(\gamma_i LS) | H | \Phi(\gamma_j LS) \rangle$ and $\mathbf{c}$ is a column vector of the mixing coefficients. For given mixing coefficients, variations in the radial function yields coupled differential equations, similar to the Hartree-Fock equations given in Eq. 3.13. The difference is that the $X(a;r)$ term arises both from the exchange of electrons within the same CSF and the interaction of electrons between different CSFs (Froese Fischer et al. 1997).

The procedure starts by estimating initial radial functions, and is followed by; i) solving the eigenvalue equation $\mathbf{Hc} = E\mathbf{c}$, ii) finding the potentials X and Y , iii) solving the MCHF equations for improved radial functions, and iv) repeating the procedure from (i) with the new radial functions determined in (iii) until the convergence. The MCHF method can be extended to determine the wavefunctions for many states at the same time. The variations are now on the weighted energy average of the targeted states and the mixing coefficients of the states are the different eigenvectors of the matrix eigenvalue equation.

3.5 Some comments on the relativistic calculations

The relativistic calculations in this thesis have been based on the multiconfiguration Dirac-Hartree-Fock (MCDHF) method, where the Hamiltonian is defined

as,

$$\mathcal{H}_{DC} = \sum_{i=1}^{N} \left(c\, \boldsymbol{\alpha_i} \cdot \boldsymbol{p_i} + (\beta_i - 1)c^2 - V_{nuc}(r_i) \right) + \sum_{i>j}^{N} \frac{1}{r_{ij}}, \tag{3.18}$$

where c is the speed of light, α and β are the Dirac matrices, $\boldsymbol{p}$ is the momentum operator, and V_{nuc} is the nuclear potential (Jönsson et al. 2017). The total orbital momentum and the spin angular momentum are coupled to the total angular momentum, $\boldsymbol{J} = \boldsymbol{L} + \boldsymbol{S}$. The wavefunction does not commute with $\mathbf{L}^2$, L_z, $\mathbf{S}^2$ or S_z, but instead with $\mathbf{J}^2$, J_z giving the angular momentum quantum numbers, J and M_J, where the latter is often suppressed in the notation. The total wavefunction can be written similar to the MCHF method as a linear combination of CSFs

$$\Psi(\gamma J) = \sum_{i=1}^{M} c_i \Phi(\gamma_i J). \tag{3.19}$$

The CSFs are built from relativistic one-electron orbitals in the form of

$$\phi_{n\kappa,m}(\mathrm{r}) = \frac{1}{r} \begin{pmatrix} P_{n\kappa}(r)\chi_{\kappa,m}(\theta,\varphi) \\ iQ_{n\kappa}(r)\chi_{-\kappa,m}(\theta,\varphi) \end{pmatrix}, \tag{3.20}$$

where $P_{n\kappa}(r)$ and $Q_{n\kappa}(r)$ are the large and small components of the radial wavefunction and $\chi_{\pm\kappa,m}(\theta,\varphi)$ are two component spin-orbit functions. The energy of a relativistic CSF can be expressed in terms of coefficients and radial integrals similar to the non-relativistic theory. By applying variational principle, one gets a set of differential equations similar to the non-relativistic case and the matrix eigenvalue equation in the form of $\mathbf{Hc} = E\mathbf{c}$. These equations can be solved in a similar way as in the non-relativistic case with additional conditions between the large and the small components of the radial functions at the origin to avoid the solutions belonging to the negative energy continuum. Once a set of radial orbitals are calculated, additional corrections can be included to account for the full relativistic effects in the configuration interaction calculation where only the expansion coefficients of the CSFs are determined. The final wavefunctions give the energy values for the fine structure states (with J quantum number), rather than LS averages. When the wavefunctions are determined, the computation of the oscillator strengths looks similar as in the non-relativistic case. More details can be found in many literature (see for example Grant 2007; Jönsson et al. 2017).

3.6 Oscillator strengths

Once the wavefunctions are known, the transition probability and the f-value of a spectral line can be computed. Let $\Psi_{\rm u}$ and $\Psi_{\rm l}$ be the wavefunctions for the upper and lower states of an E1 transition. The probability for the transition is then given in Cowan (1981),

$$A = \frac{64\pi^4 e^2 a_{\rm o}^2 \sigma^3}{3h} \sum_q |\langle \Psi_{\rm u} | E_q^{(1)} | \Psi_{\rm l} \rangle|^2 \tag{3.21}$$

where $E_q^{(1)} = \sum_{i=1}^N e_q^{(1)}(i)$ is the electric dipole operator. The electric dipole matrix element has three alternative forms. The most common forms are,

$$\langle \Psi_{\rm u} | \sum_{i=1}^N r_i C_q^{(1)}(i) | \Psi_{\rm l} \rangle \tag{3.22}$$

$$\frac{1}{(E_{\rm u} - E_{\rm l})} \langle \Psi_{\rm u} | \sum_{i=1}^N \nabla_q^{(1)}(i) | \Psi_{\rm l} \rangle \tag{3.23}$$

where $C_q^{(1)}$ denotes the renormalised spherical harmonics of rank 1 and $E_{\rm u}$ and $E_{\rm l}$ are the energy values of the u and l states (Cowan 1981). The first form is called the length form and the second one is the velocity form. Both of these forms give the same result if the exact wavefunctions are used. However, for approximate wavefunctions, the values normally differ. The agreement between the velocity and the length form are usually considered as a quality criteria of the calculations, see Section 3.8 for more details on accuracy of the calculations.

The E1 line strength, S, in the length form is defined as,

$$S = |\langle \Psi_{\rm u} | \sum_{i=1}^N r_i C_q^{(1)}(i) | \Psi_{\rm l} \rangle|^2 \tag{3.24}$$

which is independent of the wavenumber, σ. The total transition probability, A-value, becomes,

$$A \propto \sigma^3 S \tag{3.25}$$

that is dependent on the wavenumber, σ. Finally the oscillator strength is

$$f \propto \sigma S \tag{3.26}$$

which depends also on the transition energy σ. f-values calculated using the non-relativistic formalism are term averages. In Paper II, these values have been multiplied with the square of the line factor (Cowan 1981) to yield the f-values for the transitions between fine structure levels.

3.7 Systematic calculations

Calculations have been performed with the non-relativistic ATSP2K package (Froese Fischer et al. 2007) for Mg I in Paper II and the relativistic GRASP2K package (Jönsson et al. 2013, 2017) for Si I and Si II in Paper IV. Although, the relativistic effects in Si I and Si II were thought to be small, the choice of the relativistic code relied on the author's desire to learn how to use this package. After the test calculations, we realised that, in fact, these atomic systems are considerably affected by relativistic effects. For the relativistic calculations, everything described in the non-relativistic part is almost the same with a difference of relativistic orbitals. In addition, the total orbital momentum and the spin angular momentum are coupled to the total angular momentum, $\boldsymbol{J} = \boldsymbol{L} + \boldsymbol{S}$.

Both in Paper II and Paper IV, we have started with HF calculations describing the targeted states and continued with the MCHF method. Note that, in Paper IV, instead of the latter we have used MCDHF method with relativistic orbitals. For Mg I, in Paper II, the targeted states are up to $n = 7$ and $l = g$ such as from $1s^2 2s^2 2p^6 3s^2$ to $1s^2 2s^2 2p^6 3s7g$. After the test runs, we have observed that the difference between the velocity and the length form of A-values has been large for the transitions involving highly excited states, for instance states with $n = 7$. For this reason, we have included configurations with $n = 8$ and $n = 9$ in the initial HF calculations to obtain orbitals with large radii even though these configurations do not belong to our targeted states.

We have performed MCHF calculations by adding more and more CSFs to account for electron correlation. The orbitals of the targeted states have been kept fixed and CSFs have been systematically extended to orbitals with higher principle quantum numbers, n. This expansion has been done by single and double excitations with some restrictions (depending on the atomic system) from a set of reference configurations, referred as the multireference (MR), to an extended orbital set. The MR includes at least the configurations of the targeted states (including $n = 8$ and $n = 9$) but can be extended by additional important configurations.

The orbital set is extended layer by layer, which means that excitations have been allowed also to orbitals with $n+1$ and $n+2$ and so on. Similar procedures have been followed for the Si I and Si II calculations in Paper IV, i.e. adding more configurations in the MR and increasing the orbital set systematically. The accuracy of calculations depends on the size of the MR, the size of the extended orbital set to which we do excitations, and on the rule for excitations. A large MR and a large orbital set together with a less restrictive rule for excitations means large CSF expansions and this needs to be balanced against the available computational resources.

For example, to calculate the wavefunction for the $3s^2\ ^1S$ state in Mg I, as a first step we only consider $1s^22s^22p^6$ as a closed core and allow single and double excitations from the valence electrons. This type of models account for the valence-valence correlation (VV) (Froese Fischer et al. 1997) and has the form of

$$\begin{aligned}\Psi(2p^63s^2\ ^1S) = {} & c_1|(2p^63s^2\ ^1S\rangle + c_2|(2p^63s4s\ ^1S\rangle + \cdots + c_k|(2p^63s10s\ ^1S\rangle + \ldots \\ & + c_l|(2p^63p^2\ ^1S\rangle + c_m|(2p^63d^2\ ^1S\rangle + \cdots + c_o|(2p^610g^2\ ^1S\rangle + \ldots \\ & + c_p|(2p^63p4p\ ^1S\rangle + \ldots c_r|(2p^63d4d\ ^1S\rangle + \ldots c_s|(2p^69g10g\ ^1S\rangle \\ & + \ldots \end{aligned} \tag{3.27}$$

The first line represents the single excitations such that an electron from the 3s orbital moves to the 4s orbital and the second line represents the double excitations from the valence shell $3s^2$, such that two electrons in the 3s orbital move to the $3d$ orbital, and so on. In addition, the third line gives the double excitation from the 3s orbital to the 3p and 4p orbitals, and so on.

Additionally, allowing one excitation from the $2p^6$ core along with one excitation from the valence extends the model to include core-valence (CV) correlation (Froese Fischer et al. 1997). For instance,

$$\begin{aligned}\Psi(2p^63s^2\ ^1S) = {} & c_1|(2p^63s^2\ ^1S\rangle + \textit{VV excitations} \\ & + c_t|2p^53s^23p\ ^1S\rangle + c_u|2p^53s^24f\ ^1S\rangle + \ldots \\ & + c_v|2p^53s3p3d\ ^1S\rangle + c_w|2p^53s3p5g\ ^1S\rangle + \ldots \end{aligned} \tag{3.28}$$

The second line is an example of a single excitation and the third line is a double excitation accounting for the CV correlation. In the Mg I case, we have added

four orbital layers accounting for the VV and CV correlations and enlarged the number of CSFs to 2 474 744. For Si I, we have had five layers of correlation orbitals where we have accounted for the VV and the CV correlations. The number of CSFs has extended to 17 886 964. For Si II, we have expanded number of the CSFs to 11 850 176 with five layers of VV+CV correlation.

Figure 3.1 shows how the computed energy levels of Si I improve when more CSFs are added. The dashed lines show the experimental energy levels corresponding to the calculated energy levels in the same colour. Adding more CSFs improves the

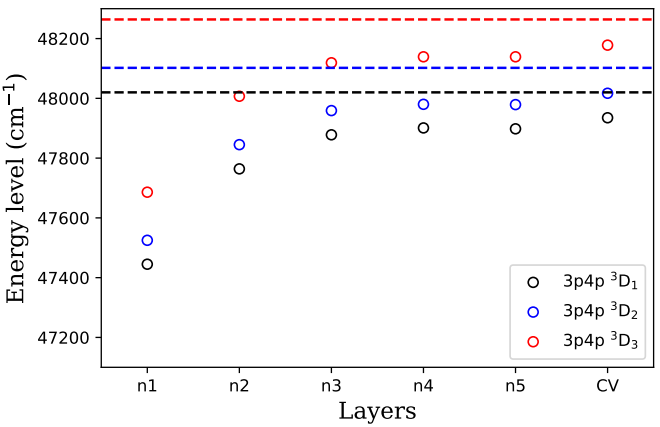

Figure 3.1: Improvement of computed energy levels in the VV correlation model as more layers of orbitals added. CV shows the energy levels when the model has been extended to include core-valence correlation. Dashed lines show the experimental energy levels for the given states.

calculations and pushes the energy values towards the experimental values. Ideally, more CSFs are desired, but there are computational limitations.

In Paper II, for the first time, we discuss the problem with the length and velocity form of the oscillator strengths. Contrary to the common knowledge, the velocity form, that weights more to the inner part of the wavefunctions, shows better convergence patterns with respect to the increasing orbital sets and is the preferred form. The same pattern has been observed for Si I and Si II in Paper IV.

The lifetime of a level is the inverse sum of all transition probabilities from that level as given in Eq. 2.4. From the computational point of view, the lifetimes can be calculated accurately as they are dominated by the strong transitions. In other words, the main contributions come from the large A-values and the weak transitions become relatively negligible.

3.8 Uncertainties

There are several accuracy indicators for the quality assessment of the calculations:

- Comparisons of lifetimes and transition probabilities (or f-values) with the experimental studies when possible.
- Comparisons of calculated energy values with the experimental energy values.
- Agreement between the length- and velocity forms.

The first and the second accuracy indicators are of course only possible to use when the experimental values are reported. Even though experimental values are reported, sometimes the uncertainties are too large to be of any practical use. For this reason, one should be aware of the quality of experiments when comparing with the calculated values. The agreement between the length- and velocity form is a necessary but not sufficient criteria for accuracy estimations (Froese Fischer 2009). In addition, one should include the energy differences in the accuracy estimations. Froese Fischer (2009) suggested that a reasonable uncertainty estimation of the transition probability is given by,

$$\delta A' = (\delta E + \delta S)A' \tag{3.29}$$

where A' is the computed transition probability, $\delta E = |E_{calc} - E_{obs}|/E_{obs}$ the relative uncertainty of the energy value, and $\delta S = |S_{len} - S_{vel}|/\max(S_{len}, S_{vel})$ the relative difference between the length- and velocity form of the linestrength. An alternative estimation was given by Ekman et al. (2014) as the relative difference of A-values in the two different forms,

$$\delta A' = \frac{|A'_{len} - A'_{vel}|}{\max(A'_{len}, A'_{vel})}. \tag{3.30}$$

In Paper II, we have estimated the uncertainties by i) comparing the calculated energy values with the experimental values, comparing the lifetimes with the experimental lifetimes when possible, ii) comparing the experimental $\log(gf)$ values

with the calculated ones, and iii) comparing the $\log(gf)$ values with the most accurate previous calculations. In Paper IV, we have done the same comparisons and in addition, we have given Eq. 3.30 values in the tables as uncertainty indicators. Figures 3.2a and 3.2b show examples of a comparison between the Mg I experimental and theoretical $\log(gf)$ values of Paper II and the relative energy value difference between the experimental and calculated values of Si I in Paper IV, respectively. The agreement in Figure 3.2a is very good except from two $\log(gf)$

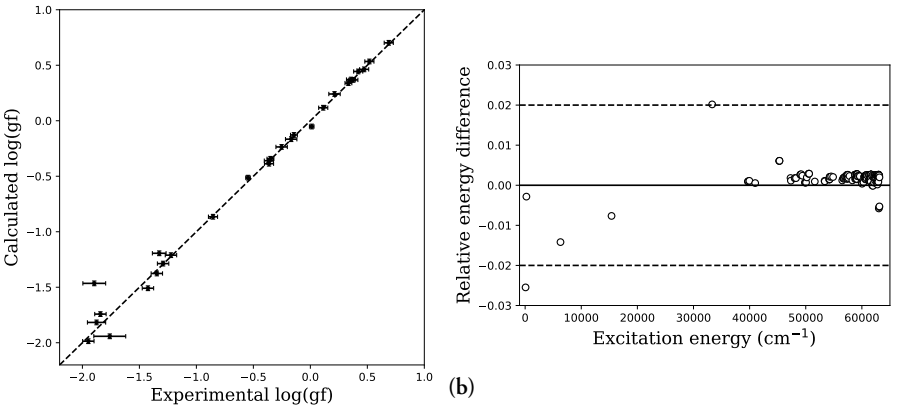

Figure 3.2: a) Comparison of the experimental and theoretical $\log(gf)$ values of Mg I lines. b) Comparison of the Si I energy value difference between the experiments and the calculated values. The dashed lines show the 2% difference.

values of Mg I on the lower part of the figure. The experimental uncertainties of these weak lines are larger than 20% due to the blending of these two lines with each other. For this reason, we recommend the calculated values. Figure 3.2b shows that the energy difference between the experimental values and the calculated values are better than 2% relative difference.

Chapter 4

Outlook

The aim of this thesis is to target radiative atomic data important for astrophysical applications. It has evolved into four papers on determining the oscillator strengths and lifetimes for Sc I, Sc II, Mg I, Si I, and Si II using high-resolution experimental measurements and high-quality calculations. As pointed out by several astronomical projects, the lack of high-accuracy data is crucial to interpret the astronomical observations (Nature 2013). The new instruments and surveys such as Gaia-ESO (Gilmore et al. 2012), 4MOST (de Jong et al. 2016), and APOGEE-2 (Zasowski et al. 2017) have been/will be observing a great number of stars that need to be analysed. Atomic data needed for analyses should match the high quality and completeness requirements, especially in the infrared region. This work is an attempt to improve and extend the set of these requested atomic data and to allow for more accurate interpretation of the astrophysical spectra.

The focus of the future projects should be on the atomic data for: i) highly excited light atoms; and ii) heavy atoms with more complicated atomic structures, such as iron group elements and neutron capture elements. It is experimentally challenging to excite high n levels and the spectra of heavy atoms look very complex. Nevertheless, careful analysis in combination with the large wavelength region coverage can overcome these problems. On the computational side, a large number of CSFs should be added to obtain highly excited levels and the electronic structure of the heavier atoms are very complicated requiring large CSF expansions. This, in turn, means that an extensive computer power with large memory is needed. New computational methodologies, such as PCFI (Verdebout et al. 2013), that decrease the number of CSFs needed for the construction of the wavefunctions, can make the calculations faster.

The traditional way of determining experimental f-values is to combine the experimental BFs with the experimental lifetimes. Unfortunately, there are not many laboratory groups left who perform experimental lifetime measurements. New projects of lifetime measurements together with the calculations will be valuable for the determination of accurate f-values.

Performing both experimental and computational methods results in a more extended set of reported atomic data. In addition, comparing two methods strengthens the accuracy of the atomic data and complements each other. Developing new projects using both methods will enhance the quality of atomic data.

Bibliography

Blackwell, D. E., Ibbetson, P. A., Petford, A. D., & Shallis, M. J. 1979, MNRAS, 186, 633

Bohr, N. 1913, Philosophical Magazine, 26, 1

Cowan, R. D. 1981, The theory of atomic structure and spectra (University of California Press: Berkeley and Los Angeles)

Davis, S. P., Abrams, M. C., & Brault, J. W. 2001, Fourier transform spectrometry (San Diego, Calif.:Academic Press)

de Broglie, L. 1925, Annales de Physique, 10, 22

de Jong, R. S., Barden, S. C., Bellido-Tirado, O., et al. 2016, in Proc. SPIE, Vol. 9908, Ground-based and Airborne Instrumentation for Astronomy VI, 99081O

Dorn, R. J., Anglada-Escude, G., Baade, D., et al. 2014, The Messenger, 156, 7

Ekman, J., Godefroid, M., & Hartman, H. 2014, Atoms, 2, 215

Engström, L. 1998, GFit, A Computer Program to Determine Peak Positions and Intensities in Experimental Spectra., Tech. Rep. LRAP-232, Atomic Physics, Lund University

Engström, L. 2014, GFit, `http://kurslab-atom.fysik.lth.se/Lars/GFit/Html/index.html`

Feltzing, S., Bensby, T., Bergemann, M., et al. 2017, ArXiv e-prints

Fock, V. 1930a, Zeitschrift fur Physik, 61, 126

Fock, V. 1930b, Zeitschrift fur Physik, 62, 795

Froese Fischer, C. 2009, Physica Scripta Volume T, 134, 014019

Froese Fischer, C., Brage, T., & Jönsson, P. 1997, Computational atomic structure - An MCHF approach (Institute of Physics Publishing, Bristol and Philadelphia)

Froese Fischer, C., Godefroid, M., Brage, T., Jönsson, P., & Gaigalas, G. 2016, Journal of Physics B Atomic Molecular Physics, 49, 182004

Froese Fischer, C., Tachiev, G., Gaigalas, G., & Godefroid, M. R. 2007, Computer Physics Communications, 176, 559

Galavis, M. E., Mendoza, C., & Zeippen, C. J. 1997, A&AS, 123, 159

Gilmore, G., Randich, S., Asplund, M., et al. 2012, The Messenger, 147, 25

Grant, I. P. 2007, Relativistic Quantum Theory of Atoms and Molecules (New York: Springer)

Gray, D. F. 2005, The Observation and Analysis of Stellar Photospheres (New York: Cambridge University Press)

Hartree, D. R. 1928, Proceedings of the Cambridge Philosophical Society, 24, 89 and 111

Hartree, D. R. 1957, The calculation of atomic structures (John Wiles & Sons, Inc., New York)

Heiter, U., Lind, K., Asplund, M., et al. 2015, Phys. Scr., 90, 054010

Huber, M. C. E. & Sandeman, R. J. 1986, Reports on Progress in Physics, 49, 397

Johansson, S. & Litzen, U. 1978, J. Phys. B: Atom. Molec. Phys., 11, L703

Johansson, S. & Litzen, U. 1980, J. Phys. B: Atom. Molec. Phys., 13, L253

Jönsson, P., Gaigalas, G., Bieroń, J., Fischer, C. F., & Grant, I. P. 2013, Computer Physics Communications, 184, 2197

Jönsson, P., Gaigalas, G., Rynkun, P., et al. 2017, Atoms, 5, 16

Kirchhoff, G. & Bunsen, R. 1860, Annalen der Physik, 186, 161

Kunze, H.-J. 2009, Introduction to plasma spectroscopy (Springer-Verlag Berlin Heidelberg)

Learner, R. C. M. & Thorne, A. P. 1988, Journal of the Optical Society of America B Optical Physics, 5, 2045

Löwdin, P.-O. 1955, Physical Review, 97, 1509

Lundberg, H., Hartman, H., Engström, L., et al. 2016, MNRAS, 460, 356

Martin, W. C. & Zalubas, R. 1980, Journal of Physical and Chemical Reference Data, 9, 1

Nature. 2013, 503, 437

Nave, G., Griesmann, U., Brault, J. W., & Abrams, M. C. 2015, Xgremlin: Interferograms and spectra from Fourier transform spectrometers analysis, Astrophysics Source Code Library

Nussbaumer, H. & Storey, P. J. 1981, A&A, 99, 177

Palmeri, P., Quinet, P., Fivet, V., et al. 2008, Phys. Scr., 78, 015304

Pasquini, L., Avila, G., Blecha, A., et al. 2002, The Messenger, 110, 1

Pauli, W. 1925, Zeitschrift fur Physik, 31, 765

Pian, E., D'Avanzo, P., Benetti, S., et al. 2017, Nature, 551, 67

Piskunov, N. E., Kupka, F., Ryabchikova, T. A., Weiss, W. W., & Jeffery, C. S. 1995, Astron. Astrophys. Suppl. Ser., 112, 525

Planck, M. 1910, Annalen der Physik, 336, 758

Pradhan, A. K. & Sultana, N. N. 2011, Atomic astrophysics and spectroscopy (Cambridge University Press: New York)

Riley, A. 2017, STIS Instrument Hanbook, Version 16.0 (Baltimore: STScI)

Rutherford, E. 1911, Philosophical Magazine, 21, 669

Ryde, N., Fritz, T. K., Rich, R. M., et al. 2016, ApJ, 831, 40

Salit, M. L., Travis, J. C., & Winchester, M. R. 1996, Appl. Opt., 35, 2960

Schrödinger, E. 1926, Annalen der Physik, 384, 361

Shetrone, M., Bizyaev, D., Lawler, J. E., et al. 2015, ApJS, 221, 24

Sikström, C. M., Nilsson, H., Litzen, U., Blom, A., & Lundberg, H. 2002, J. Quant. Spectr. Rad. Transf., 74, 355

Svanberg, S. 2001, Atomic and molecular spectroscopy : basic aspects and practical applications (San Diego, Calif.:Academic Press)

Thomson, J. 1897, Philosophical Magazine, 44, 293

Thorne, A. 1987, J. Anal. At. Spectrom., 2, 227

Thorne, A. P., Litzen, U., & Johansson, S. 1999, Spectrophysics : principles and applications (Springer-Verlag Berlin Heidelberg)

Thorsbro, B. 2016, The Near-Infrared as a Spectral Hunting Ground, student Paper

Uhlenbeck, G. E. & Goudsmit, S. 1925, Naturwissenschaften, 13, 953

Verdebout, S., Rynkun, P., Jönsson, P., et al. 2013, Journal of Physics B Atomic Molecular Physics, 46, 085003

von Fraunhofer, J. 1817, Ann. Physik, 56, 264

Zasowski, G., Cohen, R. E., Chojnowski, S. D., et al. 2017, AJ, 154, 198